IMPLEMENTATION AND EVALUATION OF A FULL-ORDER OBSERVER FOR A SYNCHRONOUS RELUCTANCE MOTOR

A Thesis
Presented to
The Academic Faculty

by

Matthew B. Hortman

In Partial Fulfillment
of the Requirements for the Degree
Master of Science

School of Electrical and Computer Engineering
Georgia Institute of Technology
April 2004

IMPLEMENTATION AND EVALUATION OF A FULL-ORDER OBSERVER FOR A SYNCHRONOUS RELUCTANCE MOTOR

Approved by:

David G. Taylor, Advisor

Thomas G. Habetler

Ronald G. Harley

Date Approved: 31 March 2004

ACKNOWLEDGEMENTS

This thesis would not have been possible without the dedicated help of my advisor, Professor David Taylor. His many hours of patient discussion, excitement for new ideas, and willingness to assist me in any way possible made this thesis an enjoyable and rewarding experience.

I would like to thank Professor Habetler and Professor Harley for their service both on my thesis committee and in the classroom.

To my wife, Beth, I owe a debt of gratitude for supporting my return to graduate school and enduring the demanding schedule it required.

I would also like to thank God for making it all possible through His grace.

Financial support was provided by the Georgia Tech Manufacturing Research Center.

TABLE OF CONTENTS

LIST OF TABLES

LIST OF FIGURES

SUMMARY

Sensorless control of the synchronous reluctance motor has been a topic of research for more than a decade, producing several successful methods to accomplish this goal. However, a technique that has been overlooked is the full-order nonlinear observer, which is essentially a software model of the motor driven by measurements from the actual motor.

Presented in this thesis is the design, implementation, and experimental testing of a full-order observer-based sensorless control technique which requires only the phase current and voltage measurements that are typically available in standard three-phase inverters.

A technique is also presented for calculating a table of observer feedback gains parameterized only by the steady-state motor speed. This allows a gain-scheduling observer to be implemented which, as shown using experiments, improves the transient response of the observer over a wide speed range.

The sensorless controller consists of a full-order nonlinear observer coupled with an input-output linearization speed controller. The resulting controller was implemented in Simulink and executed on a dSPACE DS1103 real-time DSP board using the Real-Time Workshop extension to Simulink. A custom built three-phase IGBT inverter was used to interface the DSP to a 100 watt synchronous reluctance motor for laboratory testing.

The resulting sensorless controller was able to successfully track a varying speed reference from 150 rpm to 1800 rpm with a tracking error under 5% for most of the speed range. At the lowest speeds, the tracking error begins to increase but the observer remains stable down to 150 rpm.

CHAPTER I

INTRODUCTION

The synchronous reluctance (syncrel) machine was invented by Danielson in Sweden in 1900 as an attempt to improve the power factor of the induction machine [4]. At the time, the machine was called the "self-starting synchronous machine" because of the ability to start from line current and lock into synchronous speed. These machines were built by modifying the induction machine rotor to introduce magnetic saliency, usually by removing rotor teeth. The motor soon became known as the synchronous induction machine and saw widespread use in the textile industry.

This machine was largely ignored by the research community until the late 1980s when the syncrel machine, in a form without an induction motor rotor cage, began to be considered as a feasible alternative to the induction motor for variable speed drives. It was at this time that a paper was published by T. A. Lipo entitled "Synchronous Reluctance Machines - A Viable Alternative for AC Drives" [16]. Lipo made the argument that with the improved technology in rotor design and current control, a torque density could be achieved with synchronous reluctance machines to rival the induction machine. He then challenged the reader to explore the "exciting new possibilities" offered by the syncrel machine.

Since then a variety of research has been conducted involving the syncrel motor, with a large portion focusing on sensorless operation. Sensorless control provides the ability to operate a motor using a closed-loop control system but without the need for a physical shaft position and/or speed sensor. This is advantageous in applications where the cost of the sensor, its wiring, and/or maintenance is prohibitive.

The syncrel machine is well suited to the use of sensorless control. Since there are (normally) no rotor windings or rotor cage in this type of motor, there are no unmeasurable currents (as there are in an induction motor) which must also be estimated. The syncrel motor also exhibits rotor saliency, necessary to produce reluctance torque, which causes the

motor inductance to be dependent on the shaft position and provides a way of sensing the motor position from the motor currents. In short, the syncrel motor is both a good motor and a good sensor. As a result, a variety of techniques have been developed for sensorless control of syncrel machines.

There are five principle methods available in the literature for estimating the rotor speed and/or position without a shaft sensor. The first method is the use of some type of probing pulse or measurement technique to determine the state of the rotor. For example, the technique presented in [1] takes advantage of the position dependent inductance and the coupling of the stator phases by extending the zero crossing of each current and injecting a DC current (in the dq reference frame) into two of the phases while measuring the voltage induced in the third phase.

Similarly, in [18] a probing technique dubbed INFORM (indirect flux detection by on-line reactance measurement) is used to determine the rotor position by subjecting the motor to a test voltage and observing the behavior of the current. To perform this measurement, however, the control software must disconnect the inverter from the normal task of powering the motor in order to run the diagnostic cycle.

To avoid that drawback, the authors of [5] adapted a high-frequency current injection technique, previously used with induction motors, to the syncrel motor. In this method, a high-frequency current is introduced by the current control loop and the effects on the terminal voltage are demodulated to produce a position estimate.

The second principle method, explored in [11], is to determine the speed and position by analyzing the voltage present on the neutral point of a wye-connected motor. An obvious drawback to this approach is that the motor must be connected as a wye and the neutral point must be accessible.

A third principle, used in [5] and [12], estimates the stator flux vector by integrating the difference between the motor terminal voltage and the stator resistance voltage drop. From this the rotor position can be derived. This technique works best at higher speeds where the back emf, or speed voltage, is significant. It also requires measurement of the motor terminal voltage.

Another principle method takes advantage of a side-effect induced by using a PWM inverter to deliver power to the motor. Since the inverter is delivering a square wave to an inductor, a ripple results in the motor current at the frequency of the PWM switching. By analyzing this ripple, as in [7], [17], and [18], the motor position can be derived because the amount of ripple will vary with the position dependent inductance. To obtain accurate measurements of the ripple in the current, however, measurements must be taken at a frequency at least twice as high as the PWM switching frequency.

Finally, in [6], a more control theoretic approach is taken and an adaptive controller is designed which considers the speed and position of the rotor as parameters to estimate. Although the authors targeted the permanent magnet synchronous motor in their development, it is applicable to the syncrel motor as a special case.

However, there is another technique that has been applied to other types of motors but has not yet been implemented for a synchronous reluctance motor. This approach is to use a full-order nonlinear observer to create a software model of the motor that is driven by measurements of the voltages at the terminals of the actual motor, as was done for the permanent magnet synchronous motor (PMSM) in [8]. However, a syncrel motor produces torque in a fundamentally different way than a PMSM and the success of this technique for a syncrel cannot immediately be predicted from this previous work.

This thesis explores the design and implementation of this technique and demonstrates successful operation in the laboratory using a 100 watt syncrel motor. Chapter 2 provides background information by describing the physical construction and the mathematical model of the syncrel motor. Using that model, Chapter 3 presents designs for an input-output linearization speed controller, nonlinear observer, and a sensorless controller built from them. Chapter 4 describes the laboratory setup, including inverter design and software architecture. Finally, Chapter 5 presents the experimental results.

CHAPTER II

THE SYNCHRONOUS RELUCTANCE MOTOR

2.1 Introduction

Electric machines typically use one of two different methods to convert electrical energy into mechanical energy, both of which rely on magnetism. The method used by most motor types, including DC, AC induction, and permanent magnet synchronous machines, is the interaction of two magnetic fields, one on the stator and one on the rotor. These two magnetic fields attract (or repel) each other, producing a torque on the rotor.

Alternately, a motor can be constructed based on the principle that a magnetic field will exert a force to decrease the resistance to the flow of magnetic flux (known as reluctance). In other words, the motor is based on magnets attracting metal. In these types of motors, called reluctance machines, a torque is exerted on the rotor that causes the rotor to rotate in such a way as to decrease the reluctance to the flow of magnetic flux. These types of motors do not have an "active" rotor that produces its own magnetic field. They instead have a rotor that is constructed from cleverly arranged magnetic steel that provides a position dependent reluctance (known as magnetic saliency).

Using this principle, two major types of reluctance machines have historically been developed. The first type utilizes a stator that also possesses magnetic saliency and is called the switched reluctance or stepper motor. These motors are especially common in computer controlled motion (such as printers) because they can achieve precise positioning using only open-loop control.

The second type of reluctance machine is the synchronous reluctance (syncrel) motor, which contains a smooth stator identical to that used in an AC induction motor. Syncrel motors are primarily AC machines and are usually driven using three-phase AC power. It is this type of motor that was studied for this thesis and used in the laboratory experiments.

The remainder of this chapter describes the details of the syncrel motor. Physical

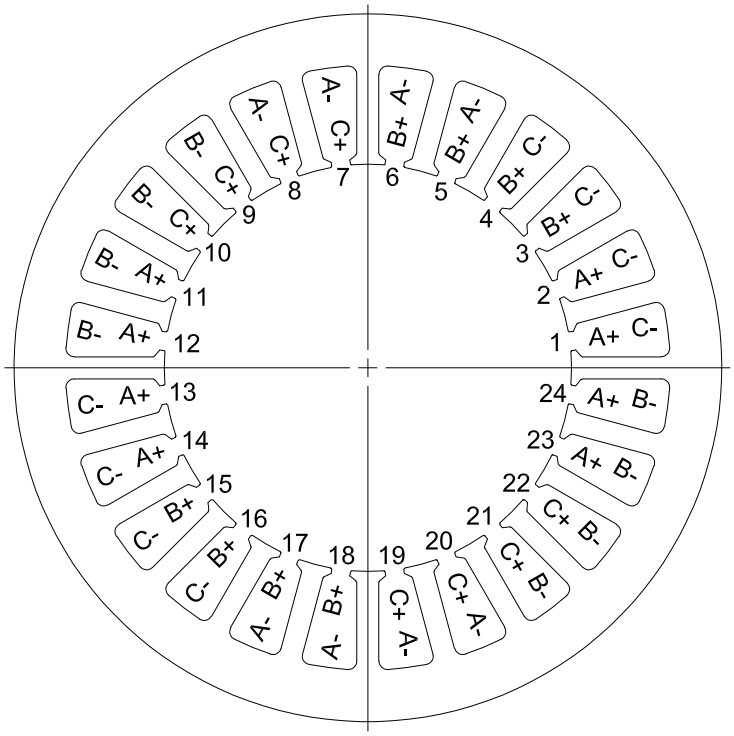

Figure 1: Three-phase syncrel motor stator.

construction is considered first as the stator and rotor designs are explored. Then the mathematical model for the motor is presented, first in the *abc* reference frame and then in the *dq* rotor reference frame.

2.2 Stator Construction

The stator of a syncrel machine is the standard smooth polyphase arrangement used in most modern AC machines. Figure 1 shows the stator from the motor used in the current research. It consists of 24 slot magnetic steel laminations on which a three-phase full pitch winding is wound. When a three-phase current is applied to the stator coils, a rotating flux wave is set up inside the stator. It is this wave that attracts the steel in the rotor and produces the reluctance torque that causes the motor to turn.

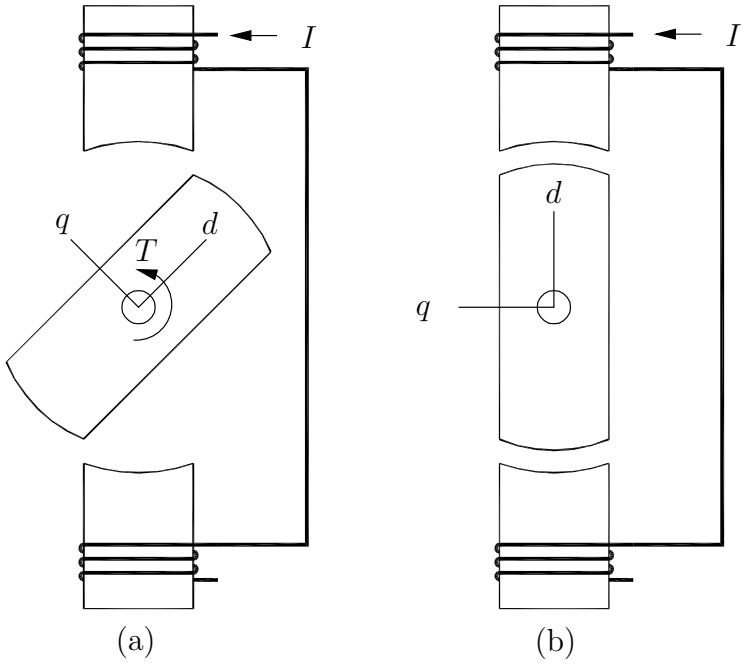

Figure 2: Basic two-pole rotor.

2.3 Rotor Construction

2.3.1 Basic Principles

The basic design principle for a syncrel rotor is to create a magnetic structure that provides minimum magnetic reluctance in one direction (called the *direct* or d axis) and maximum reluctance in the orthogonal direction (called the *quadrature* or q axis). To illustrate this concept, Figure 2 shows an oversimplified two-pole solid steel rotor in two positions along with a stator coil energized with a DC current, I. In Figure 2a, the rotor is positioned so that the stator coil is halfway between the d and q axes, providing a non-minimum reluctance path (due to the larger air gap). Due to the increased reluctance, less magnetic flux is able to flow and a torque is exerted on the rotor in a direction that will decrease the amount of reluctance.

In Figure 2b, the torque on the rotor has caused it to rotate so that the d axis is aligned with the stator coil, producing the minimum reluctance path. In this position, no torque is exerted on the rotor and the maximum magnetic flux flows through the rotor.

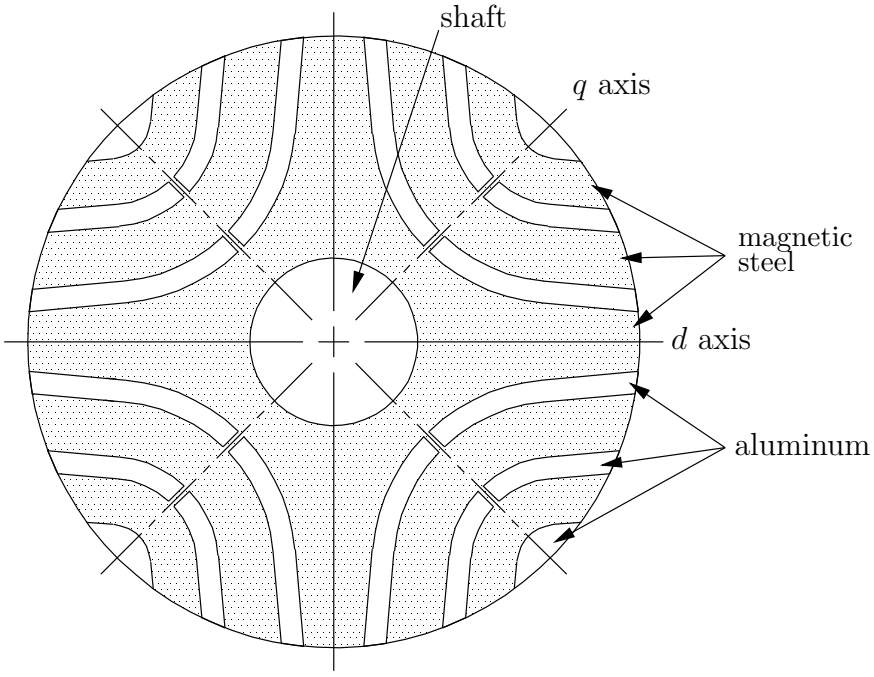

Figure 3: Transverse laminated rotor cross-section.

2.3.2 Rotor Designs

Current work on syncrel motors has focused on two similar rotor designs that differ primarily in construction technique. Both of these rotor designs are derived from the segmented rotor introduced by Lawrenson in the 1960s [13], [14].

The first type of rotor is the transverse laminated design, which can be manufactured using standard mass production techniques similar to those used for squirrel cage induction motor rotors. The individual rotor laminations are stamped out of magnetic steel and then the stack of laminations, which can be skewed to eliminate stator slot harmonics, is encapsulated in aluminum. The assembly is then machined down to the final diameter, resulting in a rotor cross-section such as that shown in Figure 3, which is from the motor used for this research. The main difference from induction rotor construction is the absence of end rings, which short circuit the rotor bars of an induction motor rotor.

The other main rotor design is the axially laminated anisotropic (ALA) design. This design has a similar cross-section to the transverse laminated design but the construction technique is vastly different. ALA rotors are built such that the laminations run axially

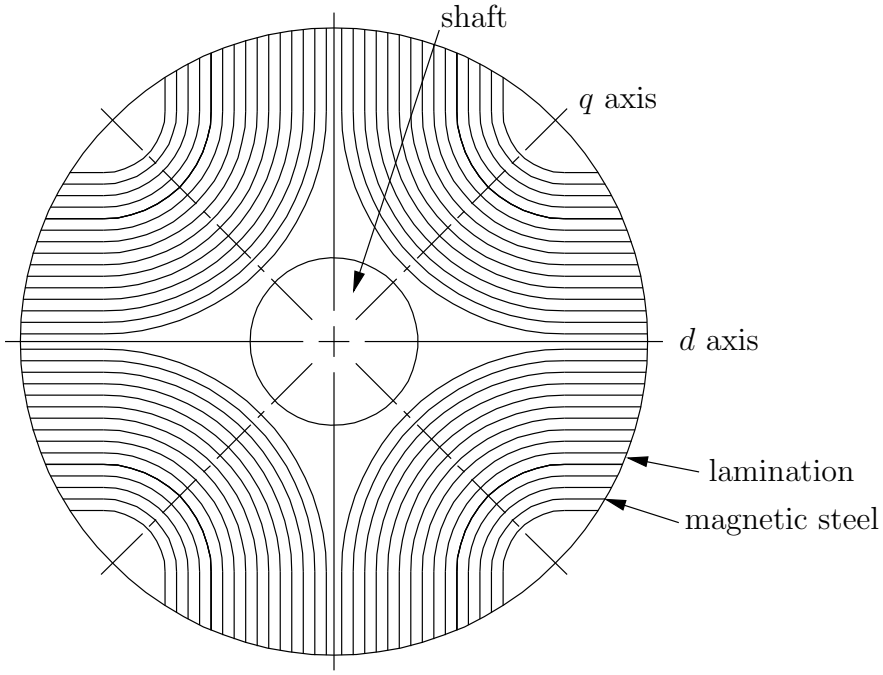

Figure 4: Axially-laminated anisotropic rotor design.

from the rotor shaft as shown in Figure 4. To construct such a rotor, sheets of magnetic steel are bent into U or V shapes and stacked together, separated by sheets of lamination material. This design has, by some reports, produced higher saliency ratios than transverse laminations, but these motors are difficult to mass produce. At this time, no manufacturer has taken up this task and all of the ALA motors used for research have been custom built.

2.4 Motor Model

As described above, the motor used in this research is a cageless, transverse laminated, four pole syncrel motor, which has no windings on the rotor of any kind (field or auxiliary) and no permanent magnets. A motor of this type produces only reluctance torque as a result of the saliency of the rotor. Figure 5 is a diagram of this motor showing both the rotor and the stator. The stator axes (a_1, b_1, c_1, a_2, b_2, c_2) denote the positive direction of the flux generated by the corresponding coils. The distributed coils of Figure 1 are shown as concentrated coils in this diagram. However, for the purposes of analysis, they are assumed to be perfectly sinusoidally distributed. The rotor d axes (d_1 and d_2) are, as before, aligned with the minimum reluctance path through the rotor. The angle θ is defined as the angle

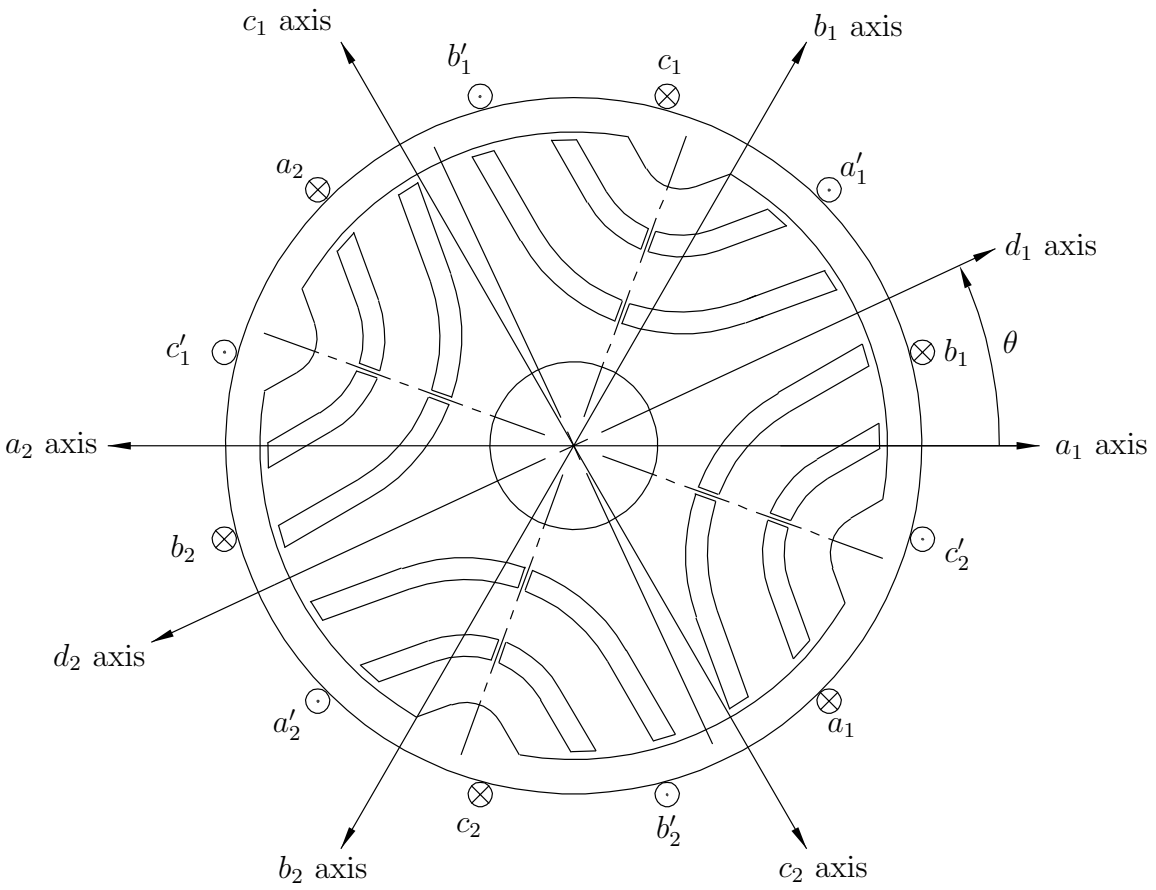

Figure 5: Syncrel axis labeling.

between the a_1 axis and the d_1 axis and will be zero when the rotor is perfectly aligned with phase a.

The coils of Figure 5 can be redrawn schematically, as shown in Figure 6, to illustrate the phase voltage connection. In this diagram, windings a_1, a'_1, a_2 and a'_2 are connected in series and combined into a single phase a winding with a voltage v_a across it and a current i_a through it. This current flows through the individual windings of Figure 5 in the directions indicated. The same relationship exists for the other two windings. Note that, although the windings are shown with a wye connection, the model presented in the following sections applies regardless of the connection between the phase windings.

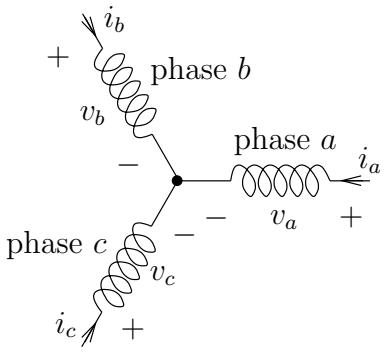

Figure 6: Syncrel motor coil schematic.

2.4.1 *abc* Reference Frame

From [10], the voltage equation of the motor in Figures 5 and 6 in machine coordinates is

$$v_{abc} = R_s i_{abc} + \dot{\lambda}_{abc} \tag{1}$$

where v_{abc} is the vector of stator phase voltages, R_s is the stator resistance, assumed to be constant, i_{abc} is the vector of stator phase currents, and, assuming magnetic linearity, the vector of flux linkages, λ_{abc}, is defined as

$$\lambda_{abc} = \mathcal{L}(\theta)\ i_{abc} \tag{2}$$

where θ is the mechanical position of the rotor, measured from the a_1 axis in Figure 5 and $\mathcal{L}(\theta)$ is the position dependent stator inductance.

If the machine inductance is also assumed to be perfectly sinusoidal, $\mathcal{L}(\theta)$ can be defined as

$$\mathcal{L}(\theta) = \begin{bmatrix} L_s & M_s & M_s \\ M_s & L_s & M_s \\ M_s & M_s & L_s \end{bmatrix} + L_m \begin{bmatrix} \cos(2N\theta) & \cos(2N\theta - \frac{2\pi}{3}) & \cos(2N\theta + \frac{2\pi}{3}) \\ \cos(2N\theta - \frac{2\pi}{3}) & \cos(2N\theta + \frac{2\pi}{3}) & \cos(2N\theta) \\ \cos(2N\theta + \frac{2\pi}{3}) & \cos(2N\theta) & \cos(2N\theta - \frac{2\pi}{3}) \end{bmatrix} \tag{3}$$

where L_s is the average stator self-inductance, M_s is the average stator mutual inductance, L_m is the variation in stator inductance due to rotor saliency, all of which are assumed to be constant, and N is the number of pole pairs in the motor.

The electromagnetic torque produced by the motor is

$$T_e = \frac{1}{2} i_{abc}^T \frac{d\mathcal{L}(\theta)}{d\theta} i_{abc} \tag{4}$$

and the mechanical dynamics of the motor are described by the equations

$$H\dot{\omega} = T_e - B\omega - T_L \tag{5}$$

$$\dot{\theta} = \omega \tag{6}$$

where H is the rotor inertia, B is the viscous friction coefficient, T_L is the load torque, and ω is the angular velocity of the motor shaft.

2.4.2 *dq* Reference Frame

The *abc* motor model, (1)-(4), is difficult to work with because of the dependence on the rotor position, θ. In order to simplify the model and remove this dependence, a change of variables is performed to transform the model into the dq reference frame. This operation effectively maps the three stator phases onto the d and q axes defined by the rotor. To effect this change of variables, the matrix

$$T(\theta) = \sqrt{\frac{2}{3}} \begin{bmatrix} \cos(N\theta) & \cos(N\theta - \frac{2\pi}{3}) & \cos(N\theta - \frac{4\pi}{3}) \\ -\sin(N\theta) & -\sin(N\theta - \frac{2\pi}{3}) & -\sin(N\theta - \frac{4\pi}{3}) \\ \frac{1}{\sqrt{2}} & \frac{1}{\sqrt{2}} & \frac{1}{\sqrt{2}} \end{bmatrix} \tag{7}$$

is applied to (1)-(4) using the equation

$$f_{dq0} = T(\theta) f_{abc} \tag{8}$$

where f_{dq0} is a vector of $dq0$ axis quantities, such as voltage, current, or flux, and f_{abc} is a vector of *abc* axis quantities. It is also useful to neglect the 0-axis quantities and define the vector notation

$$f_{dq} = \begin{bmatrix} f_d \\ f_q \end{bmatrix} \tag{9}$$

where f_{dq} can be voltage, v_{dq} or current, i_{dq}. This definition is possible because the motor in question is a balanced machine, therefore the 0-axis equation can be neglected.

The results of this transformation are the dq axis equations

$$v_d = R_s i_d - N\omega L_q i_q + L_d \dot{i}_d \tag{10}$$

$$v_q = R_s i_q + N\omega L_d i_d + L_q \dot{i}_q \tag{11}$$

$$T_e = N(L_d - L_q) i_d i_q \tag{12}$$

where v_d and v_q are the dq axis voltages, i_d and i_q are the dq axis currents, and L_d and L_q are defined as

$$L_d = L_s - M_s + \frac{3}{2}L_m \tag{13}$$

$$L_q = L_s - M_s - \frac{3}{2}L_m \tag{14}$$

The mechanical dynamics described by (5) and (6) remain unchanged.

Note that the dependence on θ has been completely removed from (10)-(12), yet they still completely describe the motor under consideration. These equations will be used in the next chapter to derive the control system.

CHAPTER III

CONTROL DESIGN

3.1 Introduction

The sensorless control scheme used in this research was designed in two distinct and independent parts. First, a nonlinear model-based speed controller was designed, using input-output linearization techniques, and then a full-order nonlinear observer was designed to provide an estimate of the rotor speed and position. Each design is based only on the model of the motor and can operate independently. These two designs are then coupled together to form a sensorless speed controller.

3.2 Speed Controller

The overall goal of the speed controller is to generate the motor voltage commands necessary for the motor shaft speed, ω, to track a given speed command, ω^*. To design this controller, input-output linearization techniques are employed. Input-output linearization is a model-based nonlinear control design technique that results in a controller which, using state feedback, cancels the nonlinearities of the plant and meets a given control objective [9]. In this case, the plant is the dq motor model presented in Section 2.4.2, reproduced below in differential form:

$$\dot{i}_d = \frac{1}{L_d}(v_d - R_s i_d + N\omega L_q i_q) \tag{15}$$

$$\dot{i}_q = \frac{1}{L_q}(v_q - R_s i_q - N\omega L_d i_d) \tag{16}$$

$$\dot{\omega} = \frac{1}{H}(T_e - B\omega - T_L) \tag{17}$$

where

$$T_e = N(L_d - L_q) i_d i_q \tag{18}$$

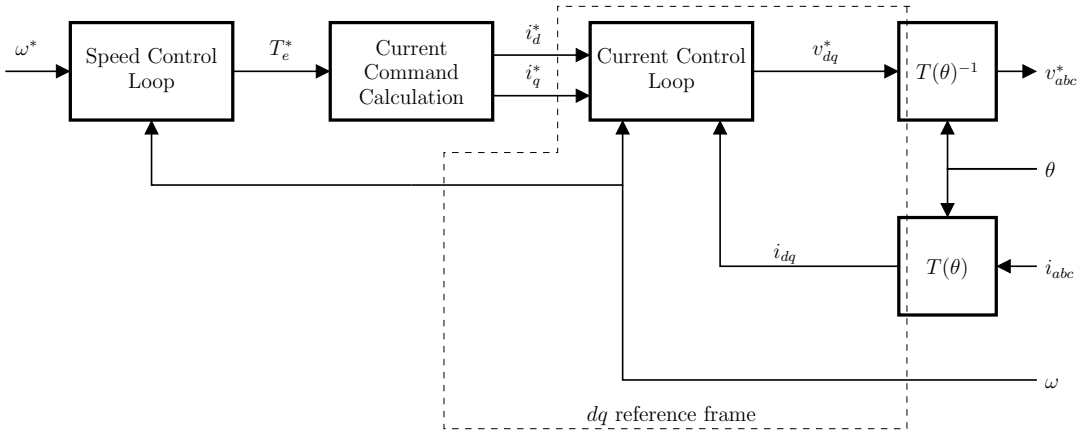

Figure 7: Speed controller block diagram.

Initially, this design is carried out as if the motor shaft speed, ω, and position, θ, as well as the phase currents, i_{abc}, are available as measurements. Later, the design is modified to accommodate the restrictions of a sensorless environment, in which ω and θ are not available.

The speed controller design consists of three components, as shown in Figure 7: a current control loop, which accepts current commands i_d^* and i_q^* and produces a motor voltage command v_{dq}^*, a current command calculation, which calculates the current commands from the torque command, T_e^*, and a speed control loop, which accepts a speed command, ω^*, and produces a torque command. Also shown in the figure are the reference frame transformations, $T(\theta)$ and $T(\theta)^{-1}$, driven by shaft position, θ, necessary to provide the dq reference frame in which this controller operates.

3.2.1 Current Loop

Torque is the fundamental quantity produced by a motor. The speed and position of the motor shaft are simply side-effects of the torque production. Therefore, it is vital to directly control the torque. This can be accomplished by controlling the current developed in the motor coils using a current control loop. Considering (15) and (16), the goal of this loop is to determine v_d and v_q such that the motor currents i_d and i_q converge to the current

commands i_d^* and i_q^*. Specifically, this design goal is for the current errors

$$\epsilon_d = i_d^* - i_d \tag{19}$$

$$\epsilon_q = i_q^* - i_q \tag{20}$$

to converge to zero as

$$\dot{\epsilon}_d = -\gamma \epsilon_d \tag{21}$$

$$\dot{\epsilon}_q = -\gamma \epsilon_q \tag{22}$$

where γ is a free gain parameter that can be used to make the current converge arbitrarily fast (within physical limits).

Taking into account the difference in time scales between the mechanical subdynamics of the motor, (17), and the electrical subdynamics of the motor, (15)-(16), the assumption can be made that the electrical subdynamics will converge significantly faster than the mechanical subdynamics. Therefore, the current commands, i_d^* and i_q^* are assumed to be constant and (21) and (22) become

$$\dot{i}_d = \gamma(i_d^* - i_d) \tag{23}$$

$$\dot{i}_q = \gamma(i_q^* - i_q) \tag{24}$$

Substituting (15) and (16) for $\dot{i}_d$ and $\dot{i}_q$ and solving for v_d and v_q, the current controller equations are obtained:

$$v_d^* = R_s i_d - N\omega L_q i_q + L_d \gamma(i_d^* - i_d) \tag{25}$$

$$v_q^* = R_s i_q + N\omega L_d i_d + L_q \gamma(i_q^* - i_q) \tag{26}$$

where v_d and v_q have been renamed v_d^* and v_q^* to represent the fact that they are commands to the motor. In each of these equations, the first two terms on the right hand side and the inductance parameter in the third term serve to cancel the nonlinearities of the electrical subdynamics and, as such, are the input-output linearization terms for this control loop.

3.2.2 Torque Control

The stated goal of the previous section was to control the torque produced by the motor. That goal, however, was not entirely accomplished. Instead, a control loop was designed

to control the direct and quadrature axis currents, not the torque. The torque produced is related algebraically to those currents by (18). Therefore, given a desired torque, (18) can be solved, non-uniquely, for the current commands. However, since one torque command must produce two current commands, a degree of freedom is available to make this decision optimally. The optimization chosen for this research is the maximum torque control (MTC) strategy described in [2] which provides maximum torque per ampere of current. This strategy yields the current commands:

$$i_d^* = \sqrt{\frac{|T_e^*|}{N(L_d - L_q)}} \tag{27}$$

$$i_q^* = i_d^* \operatorname{sgn}(T_e^*) \tag{28}$$

3.2.3 Speed Loop

The design up to this point now permits the assumption that the motor and current controller provide an ideal torque source for the speed loop design, allowing the design to only consider (17). The design goal is for the motor speed, ω, to converge to the speed command, ω^*, such that the error

$$\epsilon_\omega = \omega^* - \omega \tag{29}$$

converges to zero as

$$\dot{\epsilon}_\omega = -k\epsilon_\omega \tag{30}$$

where k is another free gain parameter that can be used to make the speed respond arbitrarily fast.

Substituting (17) and (29) into (30) and solving for T_e yields the speed control loop equation:

$$T_e^* = B\omega + T_L + H(k(\omega^* - \omega) + \dot{\omega}^*) \tag{31}$$

where T_e has been renamed T_e^* as a command to the torque/current control loop. As in the current control loop, the first two terms on the right hand side and the inertia parameter in the third term are the input-output linearization terms used to cancel the nonlinearities of the mechanical subdynamics.

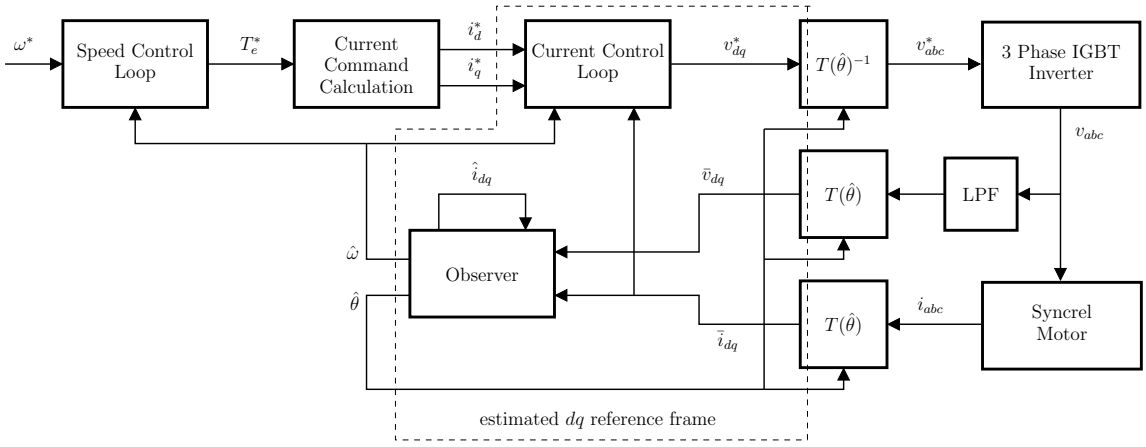

Figure 8: Sensorless speed controller block diagram.

3.3 Sensorless Speed Control

The speed controller design just completed is for a sensor-based speed controller operating in the dq reference frame. To interface this controller with the motor, the motor currents must be transformed into the dq reference frame and the commanded motor terminal voltages must be transformed back into abc, as shown in Figure 7, using the equations:

$$i_{dq0} = T(\theta) i_{abc} \tag{32}$$

$$v_{abc}^* = T(\theta)^{-1} v_{dq0}^* \tag{33}$$

Note that the zero sequence component is zero for the balanced case and is not shown in the diagram. Although not needed for this controller, measurements of the motor voltages could be transformed into the dq reference frame using the equation

$$v_{dq0} = T(\theta) v_{abc} \tag{34}$$

If the controller is operated in a sensorless environment, however, the rotor speed, ω, and position, θ, are unavailable. As a result, neither the controller itself, (25), (26), and (31), nor the reference frame transformation, (32) and (33), can be evaluated.

Instead, an observer is used, as shown in Figure 8, to provide estimates of the rotor speed, $\hat{\omega}$, and position, $\hat{\theta}$, from which an estimated dq reference frame, denoted $\overline{dq}$, can be created. To create this $\overline{dq}$ frame, (32) and (33) become

$$\bar{i}_{dq0} = T(\hat{\theta}) i_{abc} \tag{35}$$

$$v^*_{abc} = T(\hat{\theta})^{-1} \bar{v}^*_{dq0} \tag{36}$$

where the bar notation is used to indicate values in the $\overline{dq}$ reference frame. In addition, the measured motor terminal voltages, v_{abc}, must also be transformed into the $\overline{dq}$ reference frame to generate, $\bar{v}_{dq}$, which is used to drive the observer. Therefore (34) becomes

$$\bar{v}_{dq0} = T(\hat{\theta}) v_{abc} \tag{37}$$

Using the estimates provided by the observer, the speed controller for the sensorless case becomes

$$T^*_e = B\hat{\omega} + T_L + H(k(\omega^* - \hat{\omega}) + \dot{\omega}^*) \tag{38}$$

$$i^*_d = \sqrt{\frac{|T^*_e|}{N(L_d - L_q)}} \tag{39}$$

$$i^*_q = i^*_d \operatorname{sgn}(T^*_e) \tag{40}$$

$$\bar{v}^*_d = R_s \bar{i}_d - N\hat{\omega} L_q \bar{i}_q + L_d \gamma (i^*_d - \bar{i}_d) \tag{41}$$

$$\bar{v}^*_q = R_s \bar{i}_q + N\hat{\omega} L_d \bar{i}_d + L_q \gamma (i^*_q - \bar{i}_q) \tag{42}$$

which can be implemented.

3.4 Full-Order Nonlinear Observer

The final step in the design process is to develop the equations for the observer shown in Figure 8. The goal of the observer is to generate estimates of the motor speed, $\hat{\omega}$, and position, $\hat{\theta}$, using only the measurements of the motor terminal voltage, $\bar{v}_{dq}$, and motor phase currents, $\bar{i}_{dq}$, as inputs.

Because of the coupled nature of the d and q axis equations, the presentation of the observer equations can be simplified by using dq vector notation. For this reason, the following are defined:

$$\bar{i}_{dq} = \begin{bmatrix} \bar{i}_d \\ \bar{i}_q \end{bmatrix} \quad \hat{i}_{dq} = \begin{bmatrix} \hat{i}_d \\ \hat{i}_q \end{bmatrix} \quad \bar{v}_{dq} = \begin{bmatrix} \bar{v}_d \\ \bar{v}_q \end{bmatrix} \quad J = \begin{bmatrix} 0 & -1 \\ 1 & 0 \end{bmatrix} \quad L = \begin{bmatrix} L_d & 0 \\ 0 & L_q \end{bmatrix}$$

One approach to an observer might be to take a simulation approach and simply drive the motor model equations, (15)-(18), with the measured motor terminal voltages, $\bar{v}_{dq}$, and

use the resulting states as an estimate of the motor speed and position. This approach would yield the observer:

$$\dot{\hat{i}}_{dq} = L^{-1}(\bar{v}_{dq} - R_s\hat{i}_{dq} - JNL\hat{\omega}\hat{i}_{dq}) \quad (43)$$

$$\dot{\hat{\omega}} = \frac{1}{H}(N(L_d - L_q)\hat{i}_d\hat{i}_q - B\hat{\omega} - T_L) \quad (44)$$

$$\dot{\hat{\theta}} = \hat{\omega} \quad (45)$$

where $\hat{i}_{dq}$, $\hat{\omega}$, $\hat{\theta}$ are the estimates of the motor states i_{dq}, ω, and θ.

However, since this observer does not incorporate a mechanism to control the estimation errors, errors due to noise, limited precision, or inaccurate parameters will accumulate and cause the estimates to be inaccurate and unusable. This design also neglects an additional source of information about the state of the motor, the current measurements, $\bar{i}_{dq}$, and would require accurate initial conditions. Therefore, an improvement would be to use the error between the estimated currents, $\hat{i}_{dq}$, and the measured currents, $\bar{i}_{dq}$, to adjust the observer estimates. This estimated current error vector is defined as

$$\hat{e}_{dq} = \hat{i}_{dq} - \bar{i}_{dq} \quad (46)$$

and, along with gain parameters, is coupled to the observer to produce the final observer equations:

$$\dot{\hat{i}}_{dq} = L^{-1}(\bar{v}_{dq} - R_s\hat{i}_{dq} - JNL\hat{\omega}\hat{i}_{dq}) - G_{dq}\hat{e}_{dq} \quad (47)$$

$$\dot{\hat{\omega}} = \frac{1}{H}(N(L_d - L_q)\hat{i}_d\hat{i}_q - B\hat{\omega} - T_L) - G_\omega\hat{e}_{dq} \quad (48)$$

$$\dot{\hat{\theta}} = \hat{\omega} - G_\theta\hat{e}_{dq} \quad (49)$$

where

$$G = \begin{bmatrix} G_{dq} \\ G_\omega \\ G_\theta \end{bmatrix} \quad (50)$$

is the set of observer innovation gains with $G_{dq} \in \Re^{2\times2}$, $G_\omega \in \Re^{1\times2}$, and $G_\theta \in \Re^{1\times2}$.

3.4.1 Error Dynamics

One of the most important characteristics of an observer is the stability of the error dynamics. The estimation error must converge to zero rapidly in order for the estimates to

be used in closed-loop control. The observer error is defined as

$$e_{dq} = \begin{bmatrix} e_d \\ e_q \end{bmatrix} = \begin{bmatrix} \hat{i}_d - i_d \\ \hat{i}_q - i_q \end{bmatrix} \tag{51}$$

$$e_\omega = \hat{\omega} - \omega \tag{52}$$

$$e_\theta = \hat{\theta} - \theta \tag{53}$$

Substituting (5)-(6), (10)-(12), and (47)-(49) into the time derivatives of (51)-(53) yields the observer error dynamics

$$\begin{aligned} \dot{e}_{dq} &= L^{-1}\left[(e^{-JNe_\theta} - I)v_{dq} - R_s e_{dq} - JNL(e_\omega e_{dq} + \omega e_{dq} + i_{dq} e_\omega)\right] \\ &\quad -G_{dq}\left[e_{dq} + (I - e^{-JNe_\theta})i_{dq}\right] \end{aligned} \tag{54}$$

$$\dot{e}_\omega = \frac{1}{H}\left[N(L_d - L_q)(e_d e_q + i_d e_q + i_q e_d) - B e_\omega\right] - G_\omega\left[e_{dq} + (I - e^{-JNe_\theta})i_{dq}\right] \tag{55}$$

$$\dot{e}_\theta = e_\omega - G_\theta\left[e_{dq} + (I - e^{-JNe_\theta})i_{dq}\right] \tag{56}$$

where I is the identity matrix. Note that these equations include the state variables of the motor and, therefore, are dependent on the motor operating point. Note also that these nonlinear equations have an equilibrium point at the origin.

The e^{-JNe_θ} terms in (54)-(56) are a consequence of the estimated reference frame in which the observer operates. Combining (32) and (34) with (35) and (37), the relationship between the true and the estimated reference frame quantities can be expressed as:

$$\bar{v}_{dq0} = T(\hat{\theta})T(\theta)^{-1} v_{dq0} \tag{57}$$

$$\bar{i}_{dq0} = T(\hat{\theta})T(\theta)^{-1} i_{dq0} \tag{58}$$

where

$$T(\hat{\theta})T(\theta)^{-1} = \begin{bmatrix} e^{-JNe_\theta} & 0 \\ 0 & 1 \end{bmatrix} \tag{59}$$

Viewing the dq reference frame as a two-dimensional space, these equations show that the estimated reference frame quantities are "rotated" in this space by the position error, e_θ. That is, the error in the knowledge of the true reference frame causes some of the value of

$\bar{i}_d$ to be incorrectly added to (or subtracted from) $\bar{i}_q$ during the transformation from the *abc* reference frame to the $\overline{dq}$ reference frame. This error is accounted for by the e^{-JNe_θ} quantities in (54)-(56).

Because of the nonlinearities involved, further direct analysis of (54)-(56) is difficult. It is possible, however, to linearize about zero error to yield the equations

$$\dot{\tilde{e}}_o = (A_o - GC_o)\tilde{e}_o \tag{60}$$

$$\tilde{e}_o = \begin{bmatrix} \tilde{e}_d & \tilde{e}_q & \tilde{e}_\omega & \tilde{e}_\theta \end{bmatrix}^T \tag{61}$$

$$A_o = \begin{bmatrix} -\frac{R_s}{L_d} & \frac{NL_q}{L_d}\omega & \frac{NL_q}{L_d}i_q & \frac{N}{L_d}v_q \\ -\frac{NL_d}{L_q}\omega & -\frac{R_s}{L_q} & -\frac{NL_d}{L_q}i_d & -\frac{N}{L_q}v_d \\ \frac{N(L_d-L_q)}{H}i_q & \frac{N(L_d-L_q)}{H}i_d & -\frac{B}{H} & 0 \\ 0 & 0 & 1 & 0 \end{bmatrix} \tag{62}$$

$$C_o = \begin{bmatrix} 1 & 0 & 0 & -Ni_q \\ 0 & 1 & 0 & Ni_d \end{bmatrix} \tag{63}$$

which are also dependent on the operating point of the motor. The tilde notation indicates linearized quantities.

Because of this dependence on the operating point of the motor, it is quickly evident that the matrix $A_o - GC_o$ will not be full rank for zero speed operation, when all of the motor states become zero. Therefore, it cannot be used for position control or at speeds approaching zero.

Using the observer error linearization (60), Lyapunov's indirect method can be applied to the observer. As a result, if the gain G can be chosen so that the eigenvalues of (60) are in the left half plane, the observer error dynamics can be guaranteed to be locally asymptotically stable [9] and the observer estimation error will converge to zero. However, this result only applies to the observer in isolation and does not consider the rest of the closed loop system.

3.4.2 Observer Gain Selection

The observer feedback gain, G, defined in (50), must, at a minimum, be chosen so that the eigenvalues of $A_o - GC_o$ in (60) are in the left half plane in order to guarantee local stability. However, there are many possible values of G that will fulfill this goal, including, for this specific experiment, $G = 0$, but which result in poor performance and limited regions of convergence. Therefore, it is desirable to choose G optimally.

One technique used for optimal gain selection is linear quadratic optimization, which seeks a controller feedback gain K for the system $\dot{x} = A_r x + B_r u, u = -Kx$ that will minimize the cost function

$$F(u) = \int_0^\infty (x^T Q x + u^T R u) dt \tag{64}$$

where Q and R are design parameters that specify the trade-off between speed of convergence and control effort. To find the gain that will minimize $F(u)$, the algebraic Riccati equation

$$A_r^T S + S A_r - S B_r R^{-1} B_r^T S + Q = 0 \tag{65}$$

is solved for S, where Q and R are the design parameters. The gain, K, is then determined by

$$K = R^{-1} B_r^T S \tag{66}$$

This technique is implemented in the `lqr` command provided by the MATLAB control systems toolbox.

Using this technique to find the observer gain requires use of controller-observer duality which yields the system matrices

$$A_r = A_o^T \tag{67}$$

$$B_r = C_o^T \tag{68}$$

where A_o is defined in (62) and C_o in (63). Once (65) and (66) are solved to determine the controller gain, K, the observer gain, G, is then found, again using duality, by

$$G = K^T \tag{69}$$

The problem specific design parameters, Q, used to determine speed of convergence, and R, indicating the amount of control effort, are chosen to be of the form

$$Q = \alpha \begin{bmatrix} \frac{1}{\tau_{ed}} & 0 & 0 & 0 \\ 0 & \frac{1}{\tau_{eq}} & 0 & 0 \\ 0 & 0 & \frac{\beta}{\tau_m} & 0 \\ 0 & 0 & 0 & \frac{1}{4\tau_m^2} \end{bmatrix}, \quad R = \begin{bmatrix} \frac{1}{\tau_{ed}} & 0 \\ 0 & \frac{1}{\tau_{eq}} \end{bmatrix} \tag{70}$$

where $\tau_{ed} = \frac{L_d}{R}$ is the electrical time constant for the d axis, $\tau_{eq} = \frac{L_q}{R}$ is the electrical time constant for the q axis, $\tau_m = \frac{H}{B}$ is the mechanical time constant, α is a design parameter that determines the aggressiveness of the convergence, and β is a design parameter that increases the weight on the convergence time of the speed error. The structure of this matrix (with $\alpha = \beta = 1$) serves to cancel the time-scale difference between the electrical and mechanical subdynamics of the observer, thereby causing them to make equal contributions to the cost function, (64). The α design parameter is then used to decrease the convergence time and β is used to add additional weight to the convergence time of the speed estimation error, e_ω, decreasing it further and resulting in more aggressive gains, G_ω. For the present experiment, choices of

$$\alpha = 10^6, \quad \beta = \begin{cases} 100 & \text{if } \frac{30}{\pi}\Omega < 150 \\ \frac{30}{\pi}\Omega - 50 & \text{if } 150 \leq \frac{30}{\pi}\Omega \leq 550 \\ 500 & \text{if } \frac{30}{\pi}\Omega > 550 \end{cases} \tag{71}$$

provide good results, where Ω is the steady-state design speed.

To proceed with the calculation of G, numeric values for A_o and C_o are required. However, examining (62) and (63), A_o and C_o are dependent on the state of the motor. Therefore a steady-state design speed, Ω, must be chosen and the steady-state values I_d, I_q, V_d and V_q are calculated using the equilibrium equations:

$$I_d = \sqrt{\frac{|B\Omega|}{N(L_d - L_q)}} \qquad I_q = I_d \operatorname{sgn}(\Omega) \tag{72}$$

$$V_d = RI_d - N\Omega L_q I_q \qquad V_q = RI_q + N\Omega L_d I_d \tag{73}$$

These values were then substituted into A_o and C_o in place of ω, i_d, i_q, v_d, and v_q. Note that these equations assume that the currents will be equal in magnitude (not a valid assumption

in general). This condition is enforced by the torque to current calculation in (39) and (40).

The end result of this process is a method to calculate the optimum observer gains for a given steady-state speed, Ω. This speed is used to find the motor steady-state, using (72)-(73), which is substituted into (62) and (63) to find the numeric values of A_o and C_o. These values are used to find A_r and B_r using (67) and (68) so that the MATLAB `lqr` command can be used to find the solution, S, of (65), from which G is determined by (66) and (69).

For more information on linear quadratic optimization, see [15] and the documentation for the MATLAB control systems toolbox.

CHAPTER IV

LABORATORY IMPLEMENTATION

4.1 Introduction

The next step in this research was the laboratory implementation of the sensorless controller designed in the previous chapter. A block diagram of the architecture is shown in Figure 9 and explained throughout the remainder of this chapter. As shown in the figure, the entire control design, with the exception of the inverter and the motor itself, was implemented in software using a real-time DSP and a personal computer.

4.2 Software Architecture

The controller algorithms and supporting software were implemented using the Simulink® simulation language from The MathWorks, Inc. This allows both simulation directly in Simulink and automatic building of real-time DSP code using the Real-Time Workshop. Since the code-base is the same for both operations, two separate implementations of the controller are not required.

The real-time DSP code built using the Real-Time Workshop was executed on a dSPACE DS1103 DSP board installed in the host PC. This code consists primarily of the previously developed sensorless control algorithm and a test executive. The test executive provides support for setting experimental initial conditions, executing startup algorithms, generating command signals, and triggering data collection.

A major feature of the software designed for this experiment is the ability to automatically execute a sequence of tests, using various initial conditions, controller commands, and controller options, and save the resulting data for further analysis. This feature is provided, in part, by the test executive located in the real-time code. The remaining portions are provided as MATLAB scripts that execute on the PC and communicate with the code running on the DS1103 via the MLIB interface provided by dSPACE. These scripts allow

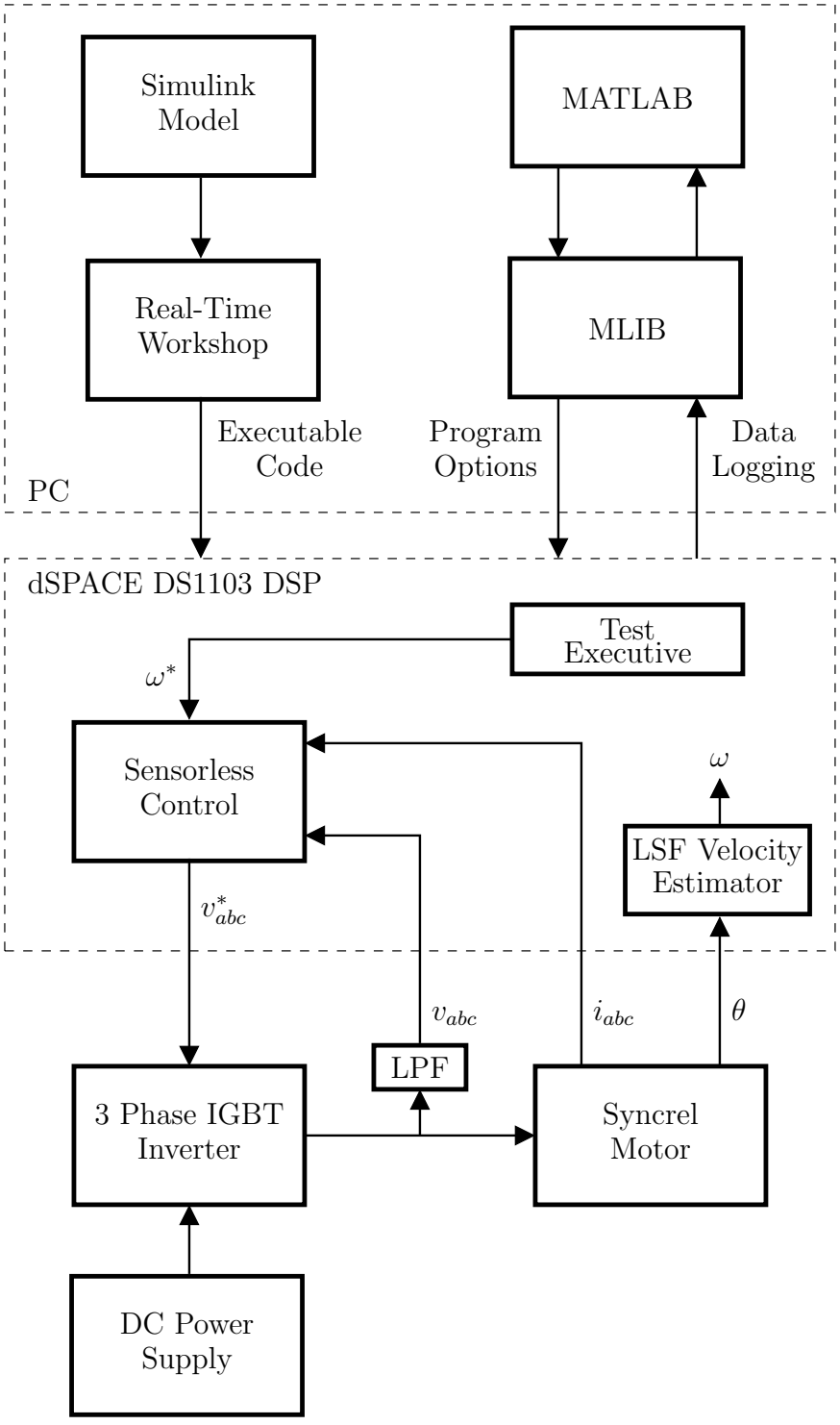

Figure 9: Laboratory implementation block diagram.

rapid collection of large amounts of experimental data covering a wide range of possible controller commands and options. For example, one test script allows the collection of a set of experimental data for every 100 rpm from 500 rpm to 1500 rpm for both the online (observer estimates used for control) and offline (observer executes in parallel but sensor measurements are used for control) configurations with no human interaction other than to approve the results of each test. This approach eliminates the mistakes that easily occur when data of this type is collected.

To communicate with the rest of the experimental setup, the DS1103 provides PWM signals which are used to control the inverter, and analog inputs, two of which are used to measure the motor phase currents and three are used to measure the motor terminal voltages, through a low-pass filter. The DS1103 also provides an encoder interface so that the actual rotor position can be measured and used for sensor-based control or monitoring of sensorless control.

To obtain a velocity measurement from the position data provided by the DS1103 encoder interface, a least-squares-fit velocity estimator from [3] is used. This algorithm, implemented as a digital FIR filter, performs an nth order polynomial fit to the last m points of data, where $n = 1$ and $m = 2$ in this implementation, and uses the derivative of the polynomial to determine the current velocity. This algorithm produces significantly better results that a simple first-backward-difference derivative, especially for the case where the period between encoder pulses is approximately the same as the sampling period for the digital controller implementation.

4.3 Inverter

A three-phase voltage-source inverter is used to generate the motor terminal voltages, v_{abc}, from the inverter command voltages, v^*_{abc}, which are encoded as PWM signals from the DS1103. The inverter was custom designed and built specifically for this experiment. As shown in Figure 10, it consists of six IRG4BC30UD IGBTs, each containing an ultrafast antiparallel diode, that are driven by an IR2131 gate driver chip, both from International Rectifier. The driver chip accepts TTL logic level inputs and provides voltage isolation,

dead time, and, using a charge pump, appropriate voltages to turn on the high-side IGBTs.

Figure 10 also shows that Hall effect current sensors are used to unobtrusively measure the current in phases a and b. These signals are then amplified, to take full advantage of the analog-to-digital converter resolution, and provided as analog inputs to the DS1103. The phase c measurement is not required as the test motor is wired in a wye connection and, therefore, the currents must add to zero. Measurements of the motor phase voltages are acquired through low-pass-filters, which remove the PWM carrier signal, and provided as analog inputs to the DS1103.

The bus voltage supply for the inverter is provided by a linear DC power supply available in the laboratory. A complete inverter schematic diagram can be found in Appendix A.

4.4 Motor

The motor used in the experiments was a 100 watt synchronous reluctance motor custom built by Motorsoft (part number 2611) for this project. The motor features an integrated digital encoder for position measurements, a thermocouple for monitoring winding temperature, and a six-wire connection so that experiments can be carried out using alternate wiring schemes. Detailed mechanical drawings of the motor, including rotor lamination and stator wiring diagrams, are available in Appendix A.

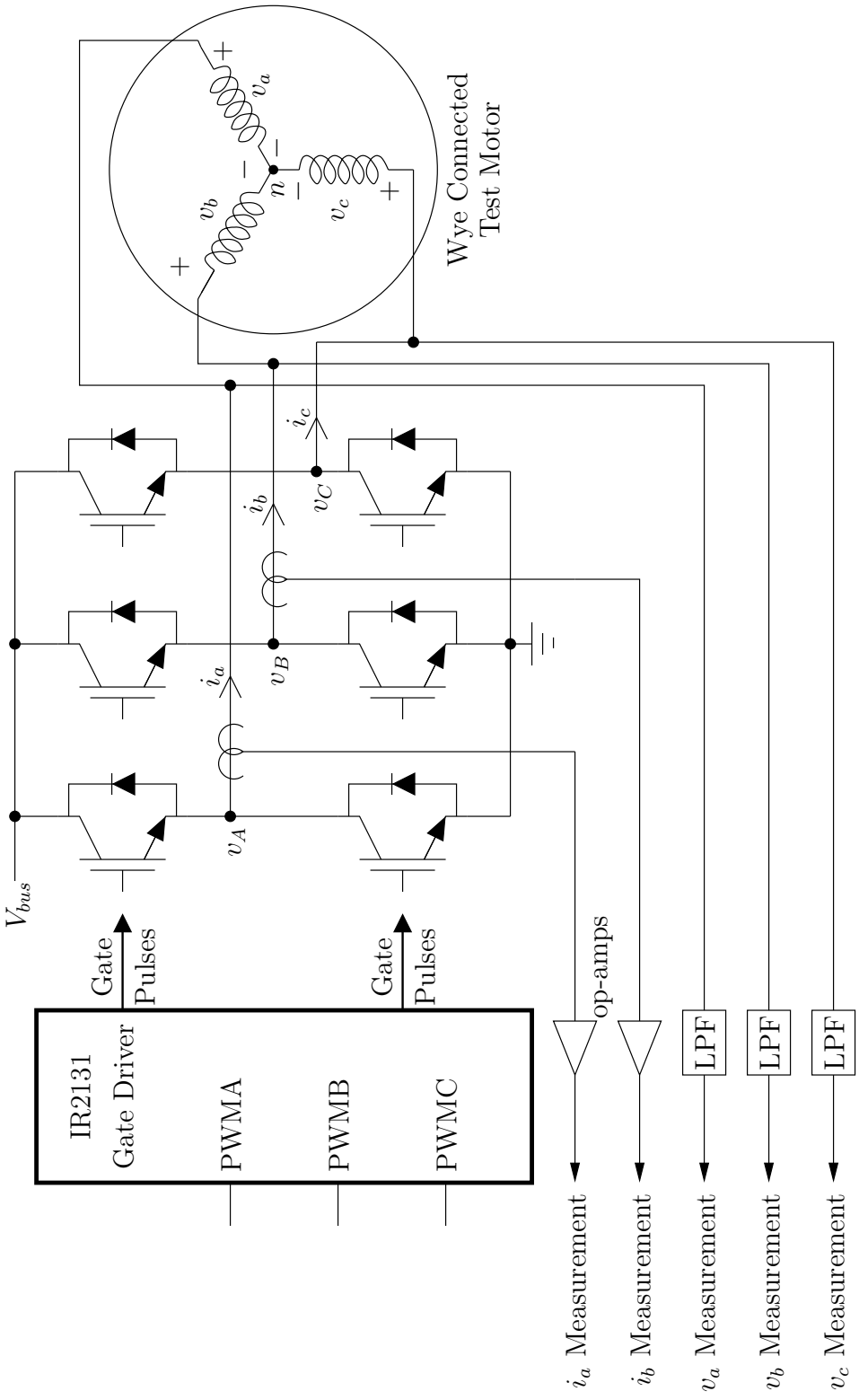

Figure 10: Three-phase voltage source inverter.

CHAPTER V

EXPERIMENTAL RESULTS

5.1 Model Characterization

The observer designed for this research is essentially a software model of the motor. As a result, it is important that the parameters of that model (R_s, L_d, L_q, H, B) be known as accurately as possible in order for the model to faithfully reproduce the response of the actual motor. Unfortunately, these parameters can vary with the speed of the motor via current, especially L_q. For this reason, the model was characterized using online tests involving all of the supporting hardware.

The first step was to determine the stator resistance, R_s. Under steady-state conditions, with the rotor stationary, the motor can be viewed as in Figure 11. The inverter is commanded to apply a DC voltage to one of the phases (phase a for this example) and, assuming $R_s = R_a = R_b = R_c$, R_s can be calculated from

$$R_s = \frac{V_a - V_b}{I_a - I_b} \tag{74}$$

The measurement is repeated at each phase and for several different voltages. The results are shown in Table 1, along with the average values. For the remaining experiments, the overall average resistance shown in the table was used as the value of the stator resistance parameter.

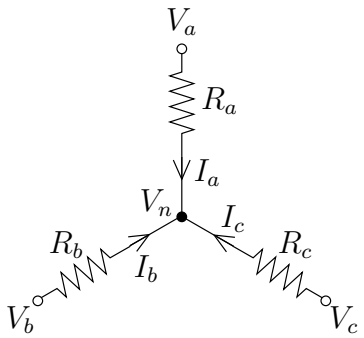

Figure 11: Effective circuit for stator resistance measurement.

Table 1: Stator resistance measurement results.

	Stator Resistance (ohms)			
Voltage (volts)	a	b	c	avg
3	0.734	0.738	0.727	0.733
4	0.745	0.754	0.729	0.743
5	0.734	0.726	0.719	0.726
6	0.749	0.750	0.714	0.738
Avg	0.740	0.742	0.722	0.735

Next, the remaining motor parameters were determined by using the sensor-based controller to produce a slow ramp up to a given steady-state speed. As an example, the motor response for 1000 rpm is shown in Figure 12. The steady-state values of v_d, v_q, i_d, i_q, and ω, denoted V_d, V_q, I_d, I_q, and Ω were determined by taking the average of the last half of the data shown in the figure. These values were then used to compute L_d, L_q, and B, assuming $T_L = 0$, using the equilibrium equations:

$$L_d = \frac{V_q - R_s I_q}{N\Omega I_d} \tag{75}$$

$$L_q = -\frac{V_d - R_s I_d}{N\Omega I_q} \tag{76}$$

$$B = \frac{N(L_d - L_q) i_d i_q}{\Omega} \tag{77}$$

where R_s is the value determined in the previous step.

Since H multiplies a derivative in the motor equations, it does not have influence over the steady-state behavior of the motor. Therefore, to calculate H, a curve fit technique was used to match the ramp response of the software motor model to the response of the actual motor.

To fully characterize the motor, the calculations were carried out over a range of speed values. The resulting calculated parameter values, along with the steady-state measurements, are shown in Table 2. From the data, it can be seen that L_q is the only parameter that shows a significant dependence on the steady-state operating point. Therefore, the value of L_q used by the sensorless controller was scheduled based on the speed command, ω^*, and the other parameters were fixed to the average values shown at the bottom of the table. This causes L_q in (39), (41)-(42), and (47)-(48) to now be a function of ω^*.

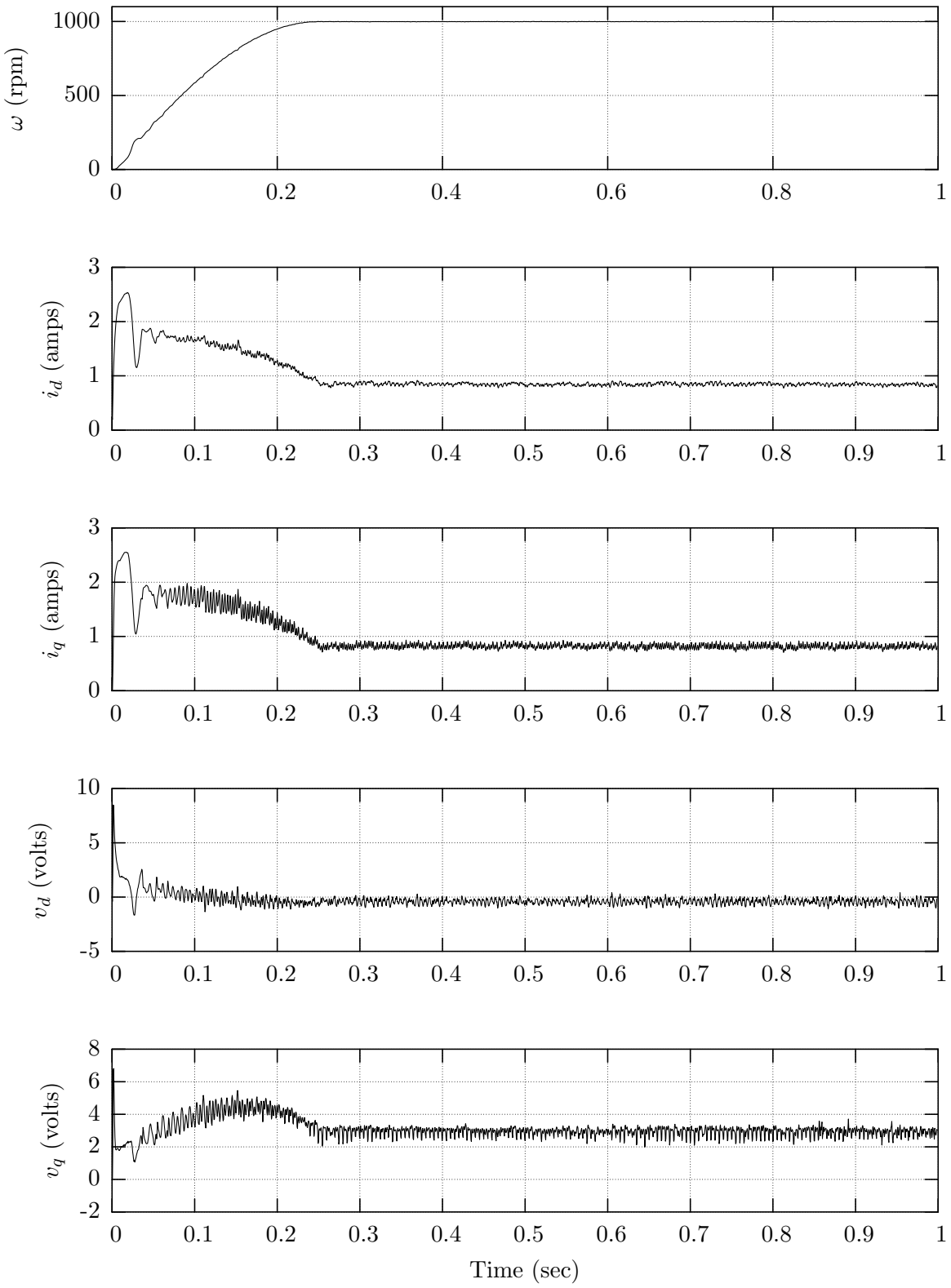

Figure 12: Motor speed, ω, current, i_{dq}, and terminal voltage, v_{dq}, while executing a smooth ramp to 1000 rpm. The steady-state values from 0.5 seconds to 1 second are used to compute the motor parameters.

Table 2: Motor steady-state values and calculated model parameters.

Steady-State Values					Model Parameters			
Ω (rpm)	V_d (volts)	V_q (volts)	I_d (amps)	I_q (amps)	L_d (mH)	L_q (mH)	H ($\mathrm{kg \cdot m^2}$)	B ($\mathrm{kg \cdot m^2 \cdot s^{-1}}$)
198.1	0.1989	0.6434	0.5510	0.5137	11.6	9.7	31×10^{-6}	53×10^{-6}
297.9	0.1376	0.9000	0.6162	0.5814	12.3	8.7	46×10^{-6}	83×10^{-6}
397.7	0.0905	1.1629	0.6740	0.6475	12.2	7.5	56×10^{-6}	99×10^{-6}
497.9	0.0155	1.4404	0.7065	0.6765	12.8	7.1	61×10^{-6}	104×10^{-6}
597.8	-0.0732	1.7123	0.7476	0.7404	12.5	6.7	62×10^{-6}	102×10^{-6}
698.2	-0.1564	2.0111	0.7712	0.7460	13.0	6.6	62×10^{-6}	100×10^{-6}
798.4	-0.2382	2.2948	0.8036	0.7800	12.8	6.4	60×10^{-6}	97×10^{-6}
898.4	-0.3142	2.6299	0.8296	0.8227	13.0	6.0	62×10^{-6}	102×10^{-6}
999.0	-0.4038	2.9264	0.8441	0.8157	13.2	6.0	60×10^{-6}	94×10^{-6}
1099.0	-0.4914	3.2279	0.8619	0.8758	13.0	5.6	61×10^{-6}	98×10^{-6}
1200.0	-0.5507	3.5606	0.8786	0.8363	13.3	5.7	60×10^{-6}	89×10^{-6}
1299.6	-0.6303	3.9436	0.9095	0.9190	13.2	5.2	62×10^{-6}	98×10^{-6}
1400.4	-0.6917	4.2587	0.9167	0.9061	13.4	5.1	58×10^{-6}	93×10^{-6}
1501.0	-0.7731	4.5026	0.9178	0.9175	13.3	5.0	58×10^{-6}	88×10^{-6}
1601.6	-0.8344	4.7867	0.9112	0.9250	13.4	4.8	59×10^{-6}	86×10^{-6}
1702.9	-0.8391	5.1755	0.9390	0.8922	13.5	4.8	58×10^{-6}	82×10^{-6}
1802.4	-0.9216	5.6031	0.9573	0.9710	13.5	4.4	60×10^{-6}	90×10^{-6}
				Average	12.9	-	57×10^{-6}	92×10^{-6}

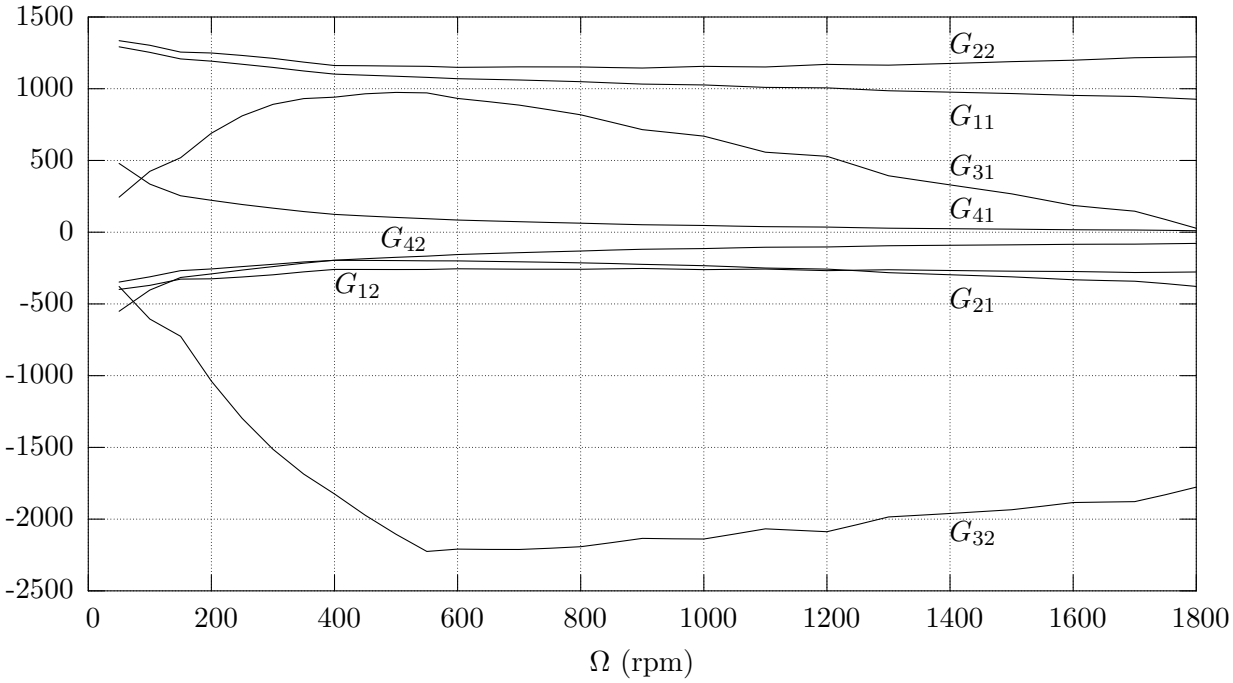

Figure 13: Calculated observer gains.

5.2 Gain Selection

To implement the sensorless controller shown in Figure 8, the gains γ and k in the speed controller and G in the observer must be chosen. The speed controller gains, γ and k, were simply chosen so that the physical limitations of the inverter power supply (current and voltage limits) were not encountered when performing a 100 millisecond smooth ramp from 0 to 1800 rpm using sensor-based control. These values are

$$k = 200 \quad \gamma = 500 \tag{78}$$

The observer feedback gain, G, defined in (50), is calculated using the motor parameters determined in the previous section and the method outlined in Section 3.4.2. This calculation was performed at 50 rpm increments in order to generate a table of gains which were then scheduled in the observer based on the speed command, ω^*, with linear interpolation used for speeds between design points. These gains are plotted in Figure 13 to show how they vary as a function of design speed. The elbow of G_{32} occurs when the value of β in (71) becomes a constant.

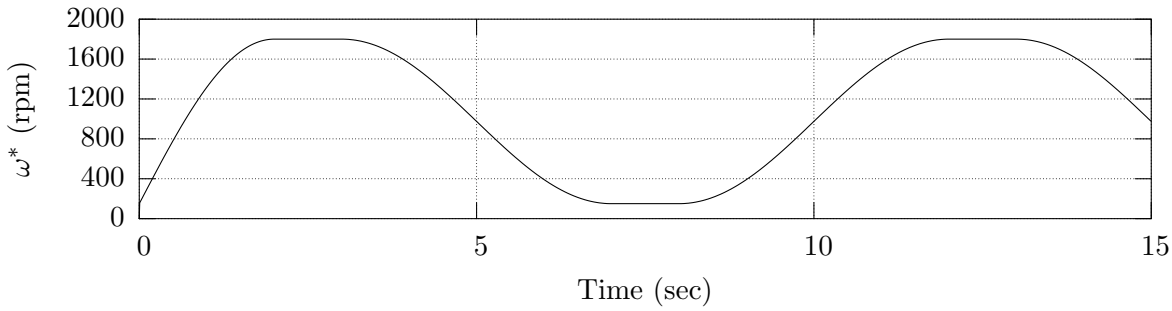

Figure 14: Speed command, ω^*, used for testing.

5.3 Sensor-based Control

In order to provide a baseline for evaluating the performance of the sensorless controller, the sensor-based controller is considered first and is commanded to follow the speed command shown in Figure 14. This command is slowly varying in order to allow the observer to converge but it covers a large speed range, from 150 rpm up to 1800 rpm, the mechanical limit of the test motor. Note that the experiment begins with an initial condition of $\omega = 150$ rpm. More details will be given during the discussion of sensorless control results.

The response of the sensor-based controller is shown in Figure 15. As expected with sensor-based control, the tracking error is minimal, under 10 rpm for the entire speed range. It does exhibit a small amount of steady-state error but this can be explained by the use of only proportional control in the speed regulation controller, (31).

5.4 Sensorless Control

The performance of the observer was evaluated in two different experiments. In the first experiment, the sensor-based controller was used to control the motor and the observer was operated offline on the data collected. In the second experiment, the observer was operated online as part of the closed-loop sensorless controller.

5.4.1 Offline Operation

The first offline experiment was simply to drive the observer with data collected from sensor-based operation while following a speed command similar to the one shown in Figure 14 but which has been scaled to have a minimum speed of 400 rpm (instead of 150). The

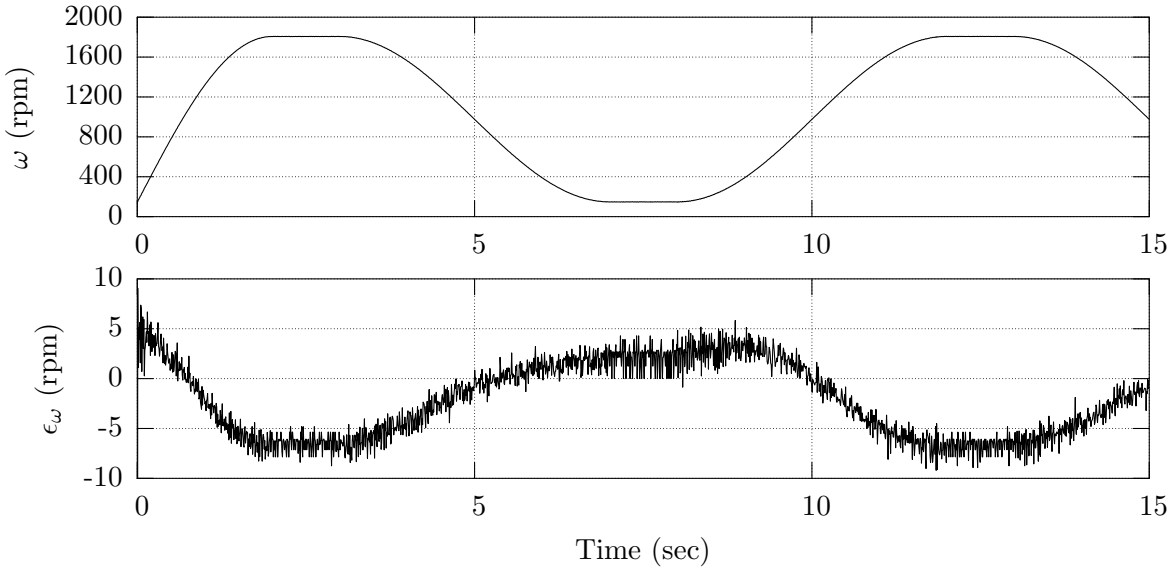

Figure 15: Actual motor speed, ω, and speed tracking error, ϵ_ω, for the sensor-based controller.

observer becomes unstable when operated below this speed and cannot track the motor speed. The observer response to this data is shown in Figure 16. The top plot shows the estimate of the motor speed generated by the observer, $\hat{\omega}$, which appears almost identical to the speed command. The middle plot shows the speed estimation error, e_ω, which is the difference between the observer's estimate of the motor speed and the actual motor speed as measured by the encoder. The speed estimation error is highest at lower speeds, when less speed voltage is available from which to drive the observer, but the maximum error is still only about 20 rpm when the actual motor speed is 400 rpm, for an error of about 5%.

The bottom plot in Figure 16 shows the observer position estimation error, which is vital because the position estimate, $\hat{\theta}$, is used to perform the transformations to and from the dq reference frame in equations (35)-(37). Inaccurate position estimates result in incorrect $\bar{v}_{dq}$ values used to drive the observer and incorrect $\bar{i}_{dq}$ values used to correct the observer. The maximum position estimation error is approximately 3 degrees.

This experiment, however, does not reveal the transient behavior of the observer, which is important for studying the effect of the gain scheduling. Therefore, another set of experiments were conducted in which the motor was operated at a constant speed by the

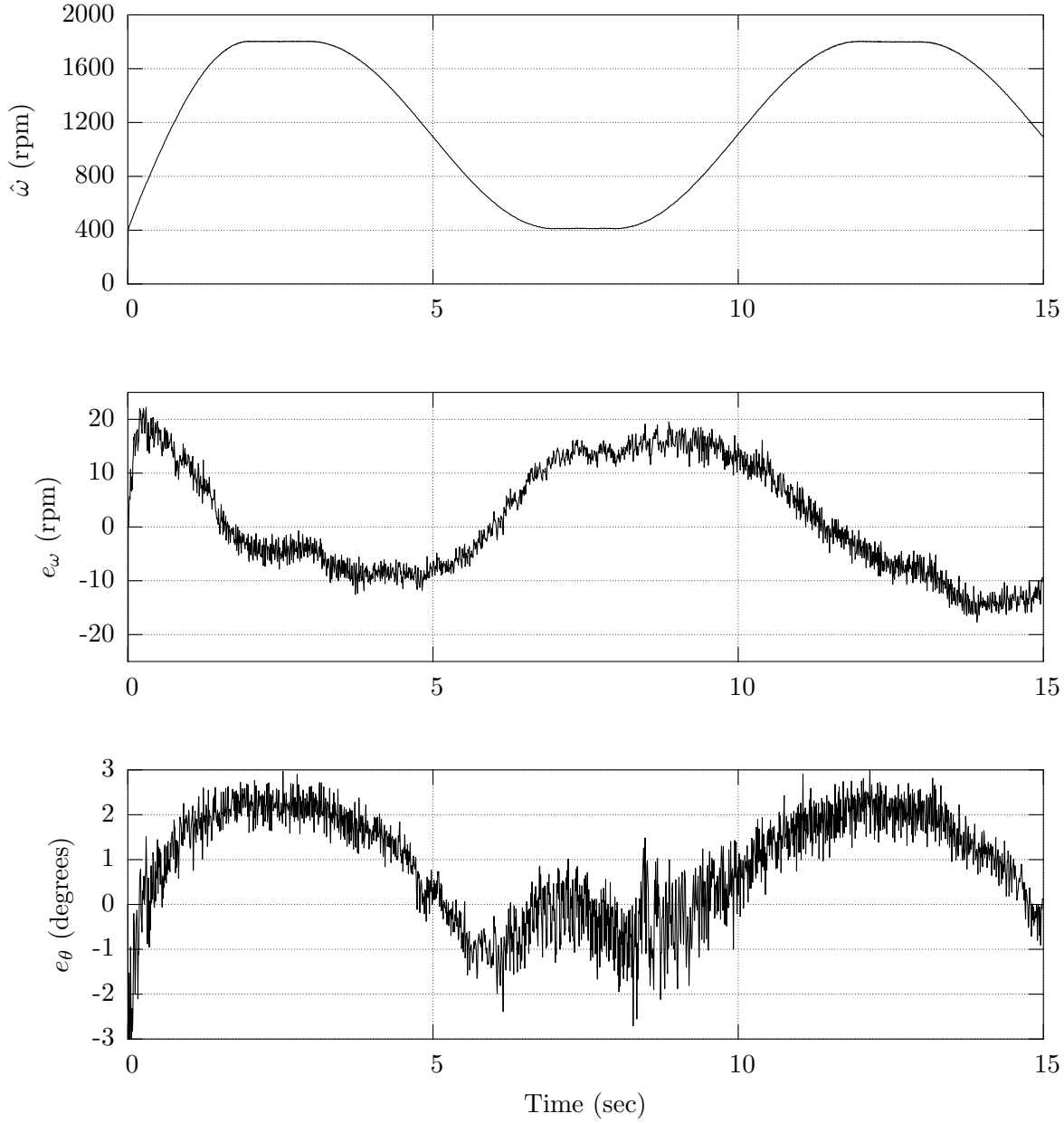

Figure 16: Motor speed estimate, $\hat{\omega}$, speed estimation error, e_ω, and position estimation error, e_θ, for offline observer operation.

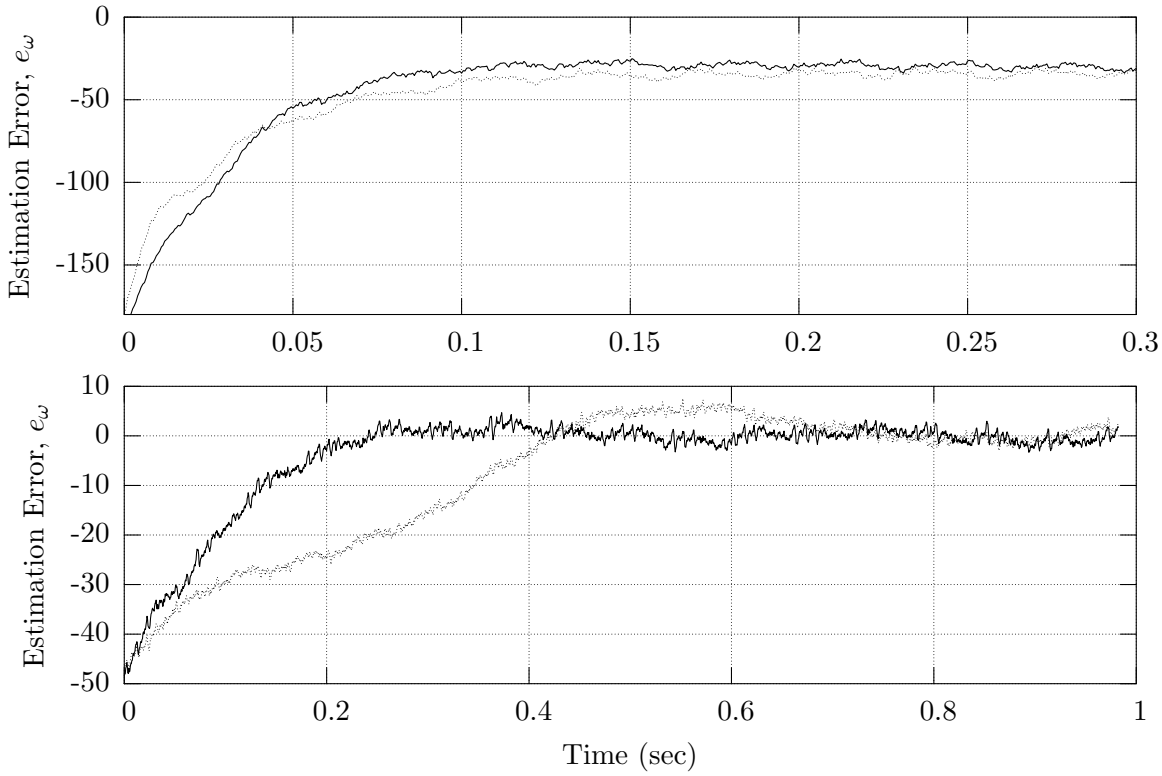

Figure 17: Transient response of the offline observer for an initial speed error of 10% and a constant motor speed of 1800 rpm (top plot) and 500 rpm (bottom plot). Shown are the fixed-gain (dotted line) and scheduled-gain (solid line) responses.

sensor-based controller and the observer was initialized with a initial speed estimation error, e_ω, of 10% of the motor speed. The transient behavior of the observer was studied for motor speeds of 1800 rpm and 500 rpm, with and without gain scheduling. For the case without gain scheduling, the fixed gains were designed for a median speed of 1150 rpm. The experiment begins after the motor has reached steady-state speed and the position, θ, is equal to zero, so that the observer position estimation error, e_θ, is initially zero.

The results of these four experiments are shown in Figure 17. The top plot shows the 1800 rpm experiment, in which the observer using gain scheduling (solid line) converges slightly faster than the fixed-gain design (dashed line). In this case, the performance suffers only slightly with fixed gains. For the 500 rpm experiment, shown in the bottom plot, however, the difference in performance is more pronounced. The fixed-gain observer exhibits a slower rise time than the gain-scheduled observer and displays significant overshoot.

Table 3: Natural frequency, damping ratio, and time constant for the observer transient experiments.

RPM	Experiment	ω_n	ζ	τ
1800	fixed-gain	70.37	1.438	0.010
	scheduled-gain	57.23	1.044	0.017
500	fixed-gain	16.25	0.470	0.131
	scheduled-gain	18.98	0.764	0.069

To help explain these phenomena, plots of the natural frequency, ω_n, damping ratio, ζ, and time constant, τ, of the two dominant observer eigenvalues for the fixed-gain and scheduled-gain cases are shown in Figure 18. Note the improved performance values, especially in damping ratio, ζ, of the gain-scheduled observer (solid line) verses the fixed-gain observer (dotted line). Note that the plots cross at 1150 rpm, the fixed-gain design speed. The decrease in performance as design speed approaches zero, most noticeable in the decrease of ω_n, is a consequence of the loss of observability of (A_o, C_o) at zero speed. The values from these plots specific to the conditions of Figure 17 are shown in Table 3.

For the 1800 rpm experiment, the fixed-gain observer has a slightly higher damping ratio, resulting in the slightly slower response compared to the scheduled-gain observer. In the 500 rpm experiment, the fixed-gain observer provides much less damping and a slower time-constant, resulting in the sluggish underdamped response.

These experiments demonstrate that gain scheduling using gains designed using the linear quadratic method described in Section 3.4.2 can be used to maintain a level of observer performance over a wide speed range that cannot be duplicated by a single fixed gain.

5.4.2 Online, Closed Loop Operation

Operating the observer offline, as in the previous experiment, demonstrates that the observer provides an effective alternative to an actual hardware encoder, which is typically used as part of a closed-loop feedback system. However, using the observer as an encoder replacement in a closed-loop system adds a level of complexity to the system because of the nonlinear nature of the observer and the controller and the interaction between the two. This interaction is difficult to predict analytically since the separation theorem from linear systems does not apply.

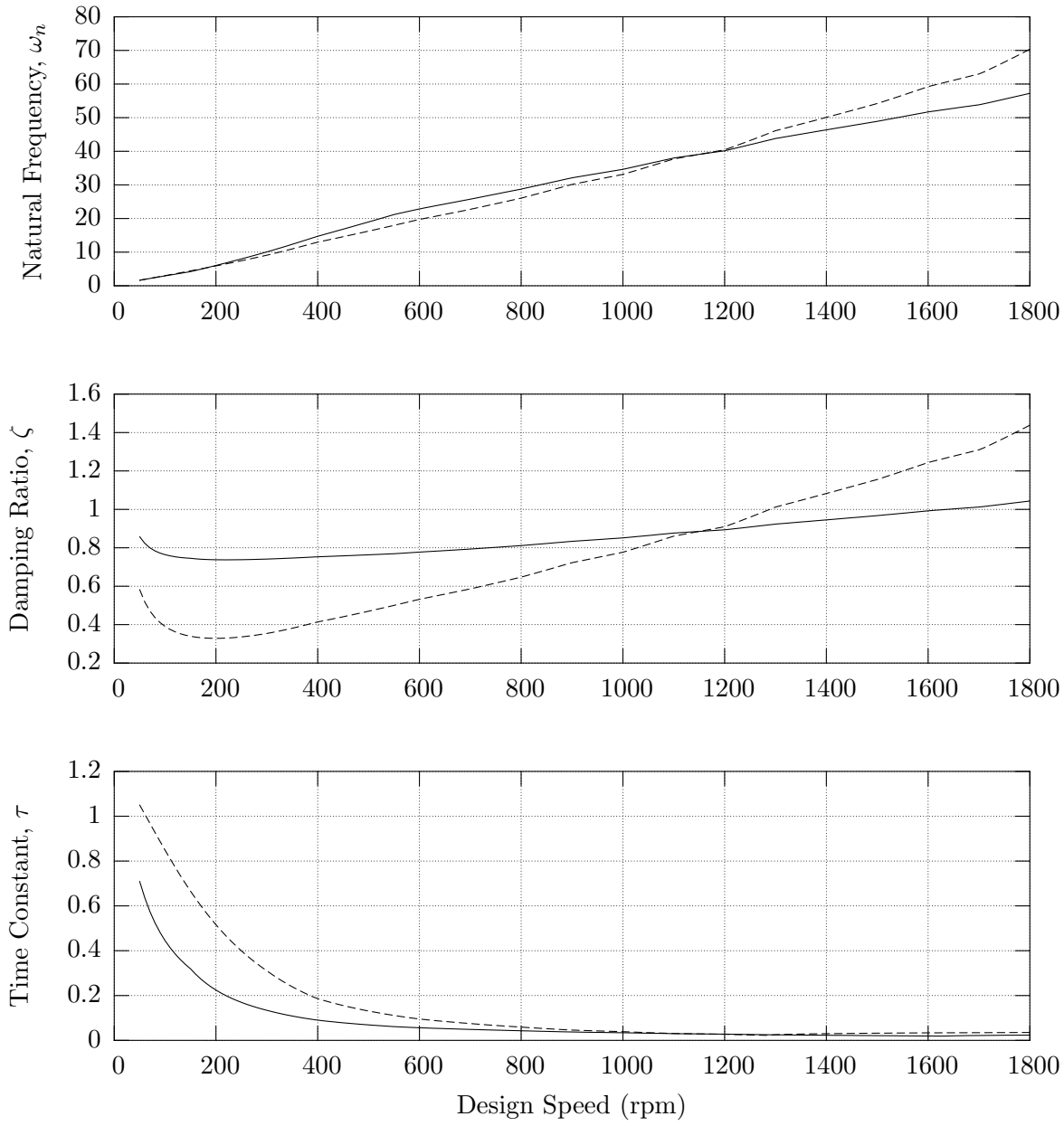

Figure 18: Natural frequency, ω_n, damping ratio, ζ, and time constant, τ, for the two dominant observer eigenvalues for fixed gains (dashed line, designed at 1150 rpm) and scheduled gains (solid line).

Therefore, an experiment was conducted in which the observer was operated in real-time and the estimates of speed, $\hat{\omega}$, and position, $\hat{\theta}$, were used directly by the speed controller in place of the same signals from the encoder. This closed-loop sensorless system is evaluated by commanding it to follow the speed trajectory shown in Figure 14. Note that this trajectory begins at 150 rpm, not zero. Because of the loss of observability at zero speed and the poor performance at low speeds, the observer cannot be used to control the motor from stand-still. Instead, another algorithm must be used to get the motor up to speed. As the goal of this research was to evaluate the observer, not to build a practical, full-range control system, the sensor-based controller was used to bring the motor to an initial speed of 150 rpm. Once that speed was reached, the test executive activated the sensorless controller when the rotor position reached zero degrees. This ability to control the experimental initial conditions was vital to performing experiments with this observer. If a practical implementation were sought, some form of open-loop control could be used to bring the motor into a speed range where the observer could take over.

Figure 19 shows the response of the sensorless controller to this varying speed command. The first plot shows the actual motor speed while under sensorless control and the second plot shows the tracking error, ϵ_ω, which is the difference between the actual motor speed and the commanded speed from Figure 14. The motor exhibits smooth ramps between speeds but, during the constant speed portions of the speed command, the motor exhibits an oscillation in speed. The tracking becomes worse at the lower speeds but this is expected because of the low speed characteristics of the observer error dynamics.

Figure 19c shows the observer estimation error during this experiment. Comparing this plot with Figure 19b, observer estimation error is almost entirely responsible for the tracking error of the overall system. In other words, the speed controller portion of the system is performing accurately but is hampered by incorrect estimates of the motor state.

Finally, Figure 19d shows the observer position estimation error, e_θ. Again, this error measure is important because the position estimate, $\hat{\theta}$, is used to create the estimated reference frame, $\overline{dq}$, in which the observer and speed controller operate. From the figure, the observer position estimate is minimal except when the motor speed is low. At the lower

speeds, the estimated reference frame becomes increasingly inaccurate and this contributes to the speed estimation error.

Note that the speed command followed during this closed-loop experiment extends down to a speed of 150 rpm while the open-loop observer exhibited instability at speeds lower than 400 rpm. This result indicates that operating the observer in a closed-loop system actually has a *stabilizing* effect on the observer, allowing closed loop operation at lower speeds than open loop.

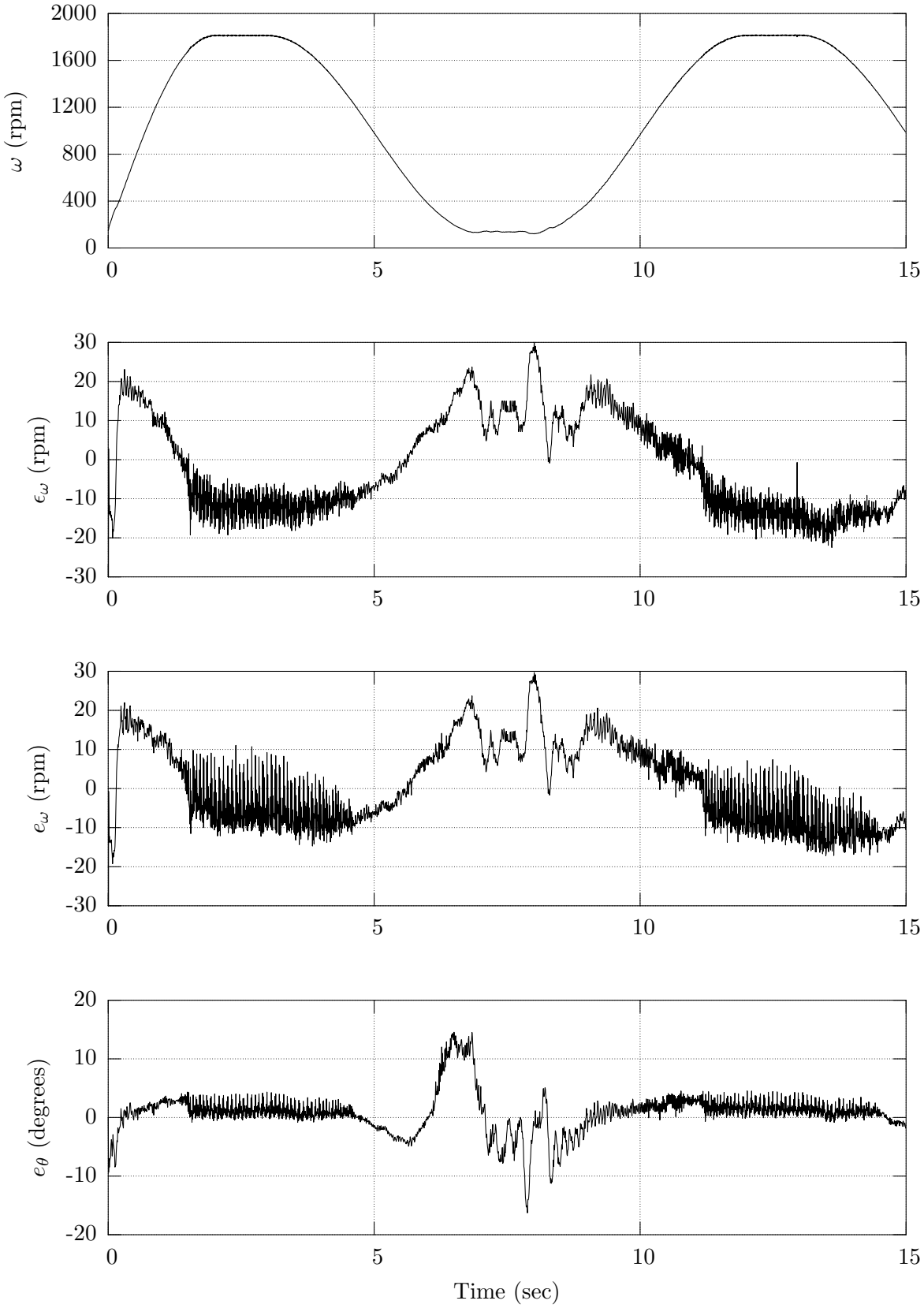

Figure 19: Actual motor speed, ω, speed tracking error, ϵ_ω, speed estimation error, e_ω, and position estimation error, e_θ, for the closed-loop sensorless controller.

CHAPTER VI

CONCLUSIONS

This thesis has shown that successful sensorless control of a synchronous reluctance motor can be accomplished using a full-order nonlinear observer which relies only on measurements of the motor phase currents and terminal voltages. Coupled with a two-loop speed controller designed using input-output linearization, closed-loop sensorless control was demonstrated by following a varying speed command from 150 rpm to 1800 rpm. The experiment also revealed a surprising result in that closing the loop actually *stabilized* the observer. That is, the observer maintains accurate estimates of the motor states at lower speeds in closed-loop operation than when operated offline.

A systematic method for calculating the observer feedback gains has also been presented. This method is based on linear-quadratic optimization and provides a way to calculate a table of observer gains based on a single parameter, the steady-state design speed. Using this table of gains, a gain-scheduled observer was implemented which was shown, through experiments, to improve the transient response of the observer to estimation error and, therefore, provide a more uniform response across the speed range.

The resulting sensorless control system performed well when commanded to follow a varying speed reference, with a tracking error under 5% for most of the speed range. The performance, while degraded at lower speeds, was adequate for many applications such as driving pumps or fans. In these applications, the efficiency gain of sensorless field oriented control, which requires knowledge of the rotor position, over pure open-loop operation may give the syncrel motor the advantage necessary to become a superior solution for the application.

As with any research project, ideas and directions for future research have been revealed over the course of completing this work. A number of which are:

- Improve observer gain calculation to decrease the convergence time.

- Improve low speed performance.
- Develop a companion algorithm to handle motor startup and handoff to the sensorless controller.
- Develop an adaptive observer that can also estimate the parameters of the motor.
- Develop an excitation signal that can be used to prevent the loss of observability at zero speed.

APPENDIX A

ADDITIONAL LABORATORY DETAILS

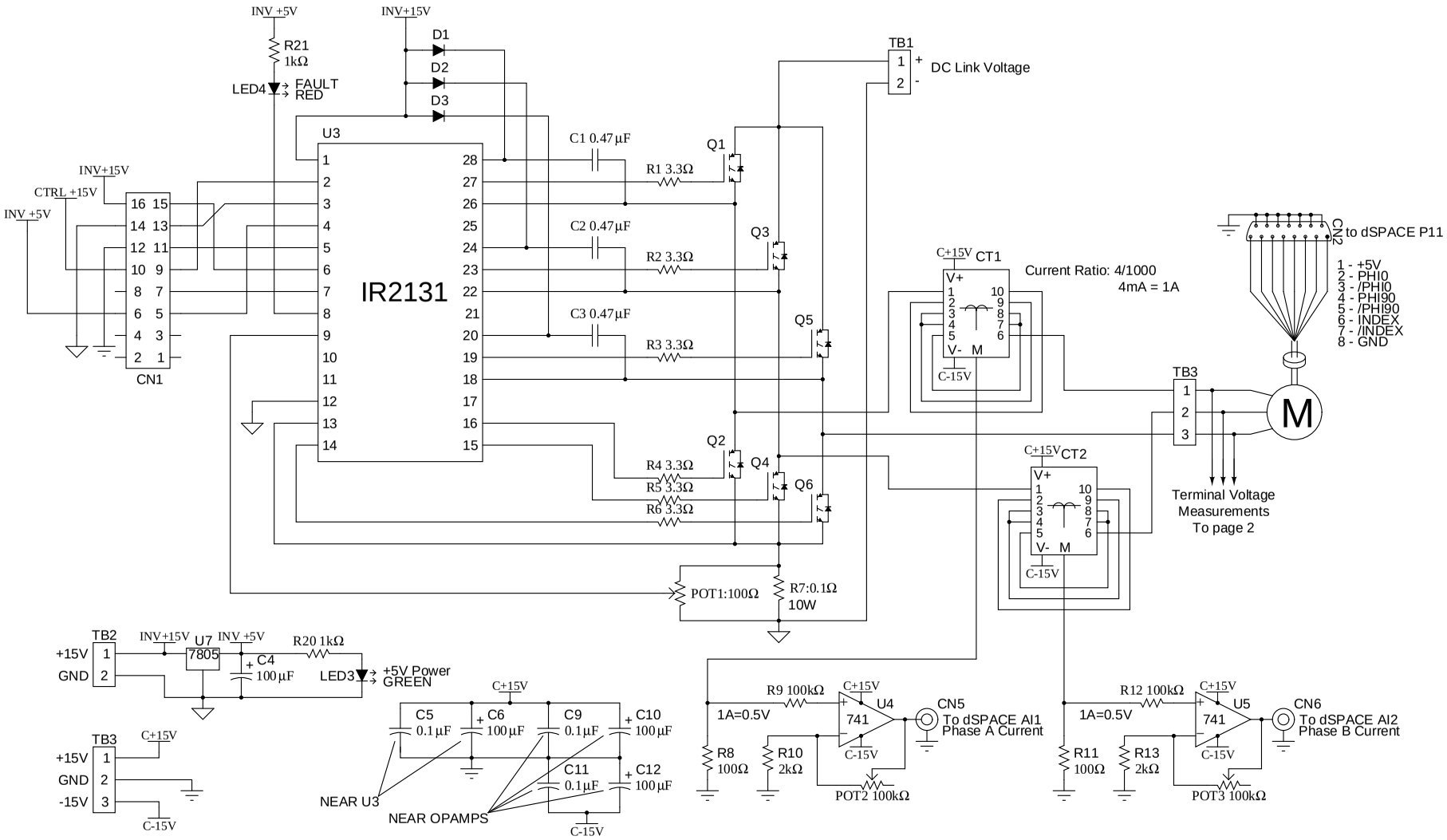
INV +5V
INV+15V
R21
1kΩ
LED4
FAULT
RED
D1
D2
D3
U3
IR2131
C1 0.47µF
C2 0.47µF
C3 0.47µF
R1 3.3Ω
R2 3.3Ω
R3 3.3Ω
R4 3.3Ω
R5 3.3Ω
R6 3.3Ω
Q1
Q2
Q3
Q4
Q5
Q6
CTRL +15V
CN1
TB1
DC Link Voltage
CT1
CT2
Current Ratio: 4/1000
4mA = 1A
C+15V
C-15V
V+
V-
M
CN2
to dSPACE P11
1 - +5V
2 - PHI0
3 - /PHI0
4 - PHI90
5 - /PHI90
6 - INDEX
7 - /INDEX
8 - GND
TB3
Terminal Voltage
Measurements
To page 2
POT1:100Ω
R7:0.1Ω
10W
TB2
+15V
GND
U7
7805
C4
100µF
R20 1kΩ
LED3
+5V Power
GREEN
C5
0.1µF
C6
100µF
C9
0.1µF
C10
100µF
C11
0.1µF
C12
100µF
NEAR U3
NEAR OPAMPS
-15V
R9 100kΩ
R8
100Ω
R10
2kΩ
U4
741
POT2 100kΩ
CN5
To dSPACE AI1
Phase A Current
1A=0.5V
R12 100kΩ
R11
100Ω
R13
2kΩ
U5
POT3 100kΩ
CN6
To dSPACE AI2
Phase B Current

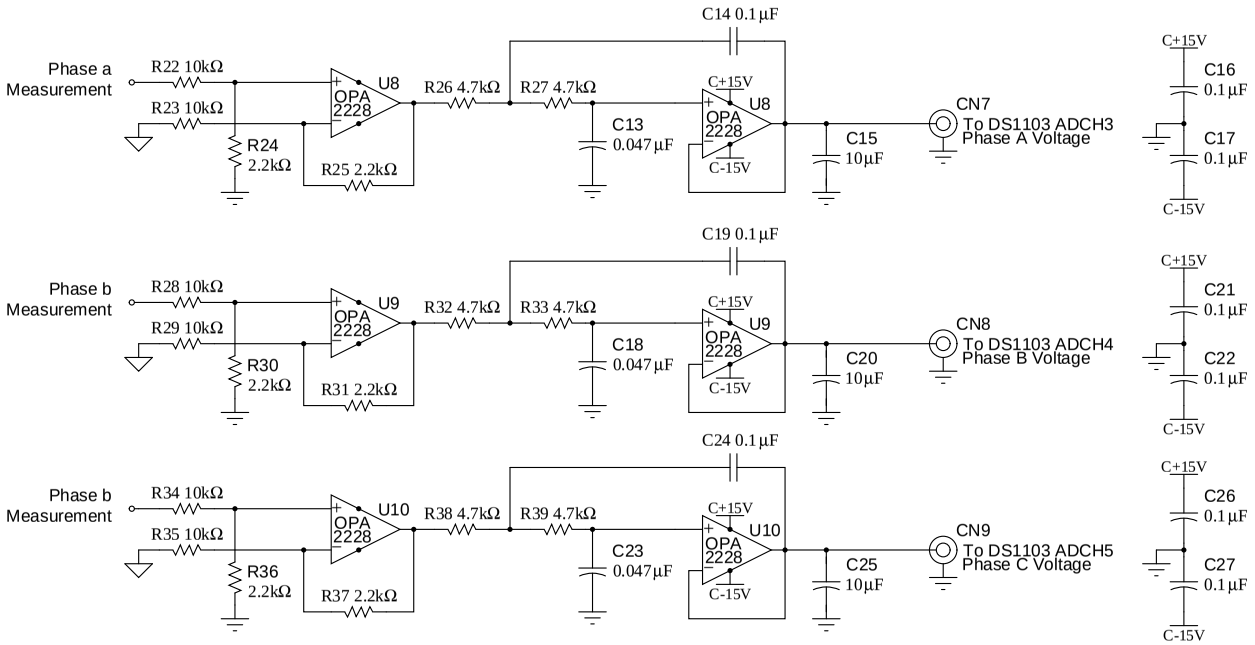
Phase a Measurement
R22 10kΩ
R23 10kΩ
R24 2.2kΩ
R25 2.2kΩ
U8
OPA 2228
R26 4.7kΩ
R27 4.7kΩ
C14 0.1µF
C13 0.047µF
C+15V
C-15V
C15 10µF
CN7
To DS1103 ADCH3
Phase A Voltage
C16 0.1µF
C17 0.1µF
Phase b Measurement
R28 10kΩ
R29 10kΩ
R30 2.2kΩ
R31 2.2kΩ
U9
R32 4.7kΩ
R33 4.7kΩ
C19 0.1µF
C18 0.047µF
C20 10µF
CN8
To DS1103 ADCH4
Phase B Voltage
C21 0.1µF
C22 0.1µF
Phase b Measurement
R34 10kΩ
R35 10kΩ
R36 2.2kΩ
R37 2.2kΩ
U10
R38 4.7kΩ
R39 4.7kΩ
C24 0.1µF
C23 0.047µF
C25 10µF
CN9
To DS1103 ADCH5
Phase C Voltage
C26 0.1µF
C27 0.1µF

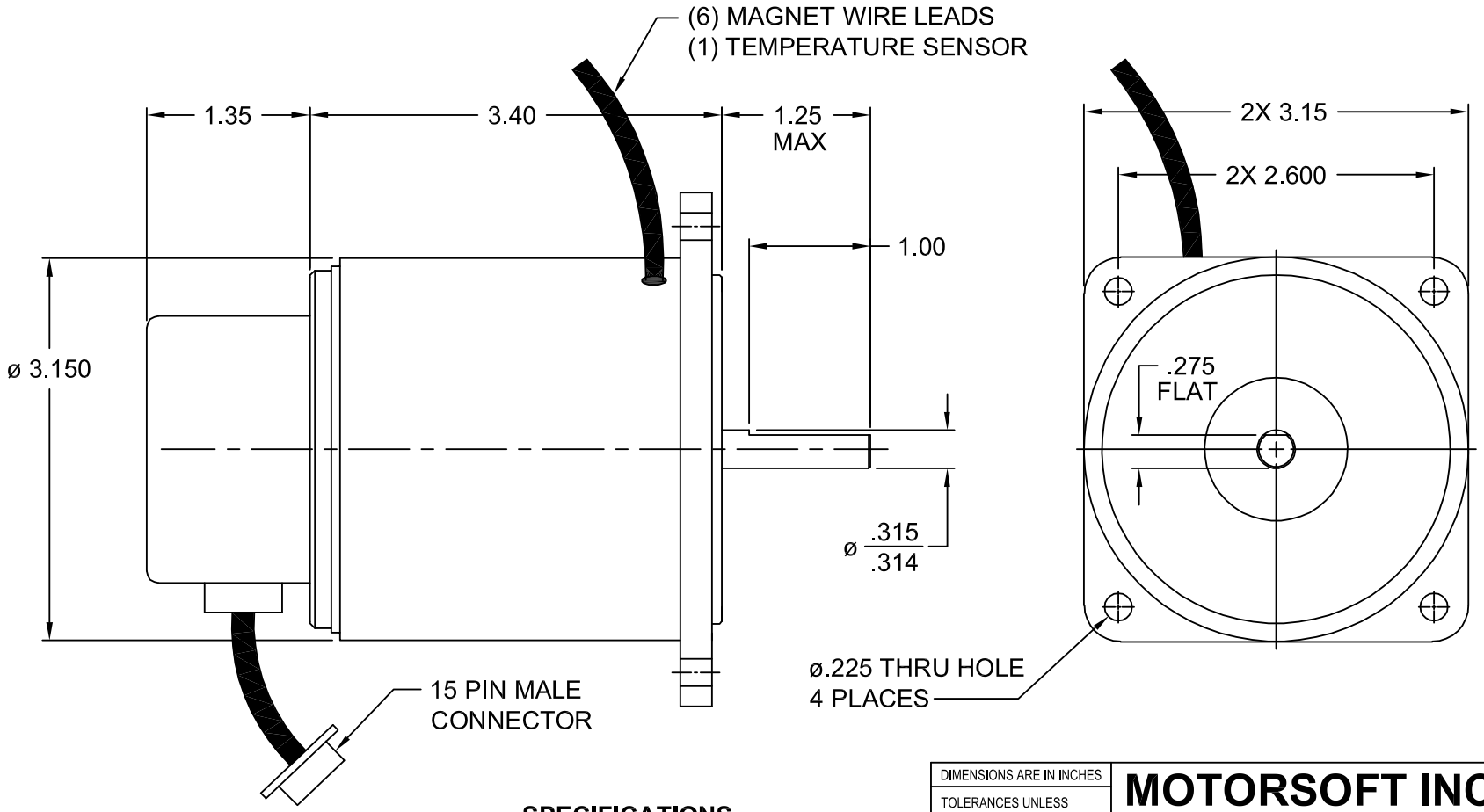

SPECIFICATIONS

RATED VOLTAGE - 36

RPM - 1800 MAX

DIMENSIONS ARE IN INCHES TOLERANCES UNLESS OTHERWISE SPECIFIED .XX = ±.005 .XXX = ±.001 ANGLE = ± 0° 30'	**MOTORSOFT INC.**				
	DWG	S.E.M.	9-19-01	TITLE SYNCHRONOUS RELUCTANCE MOTOR OUTLINE	
	CHK	JRH	10-4-01		
USED ON	APPD	JRH	10-4-01		
	SCALE 1 : 1			DWG. 2611	REV —

REV	ECO NO.	DATE	BY	APPD.
A	R0169	8/22/02	SEM	JRH

CENTER *	
A	4X R 12.12
B	4X R 10.69
C	4X R 7.10
D	4X R 5.67
E	4X R 2.68

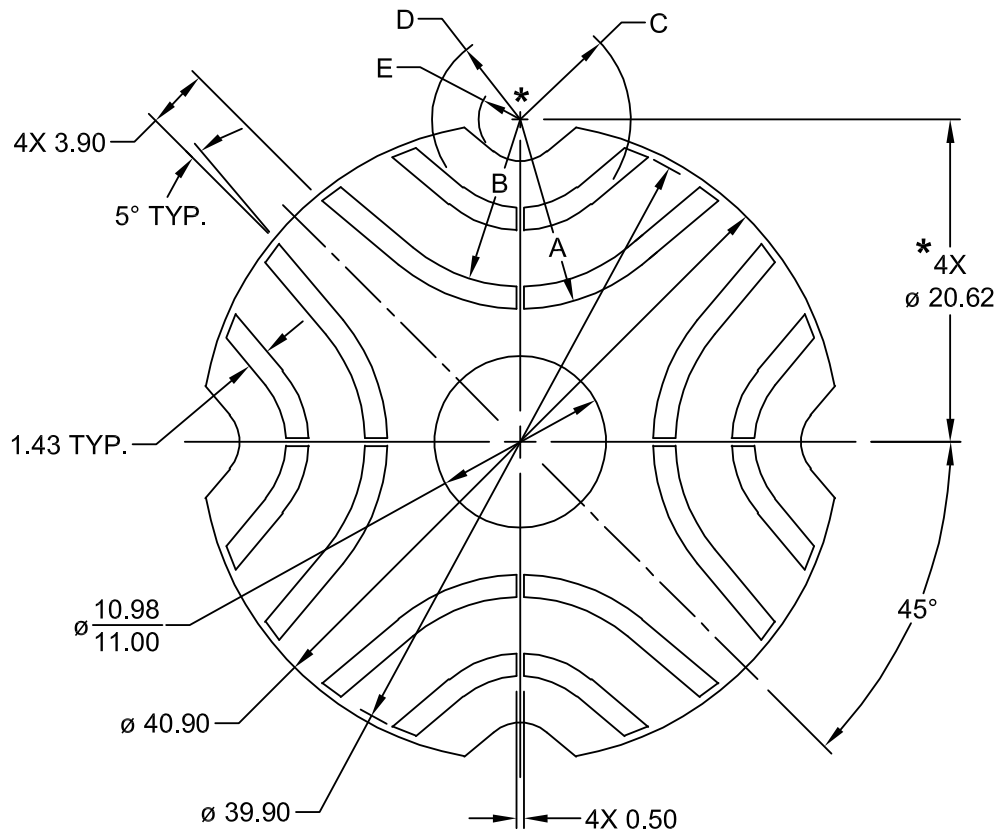

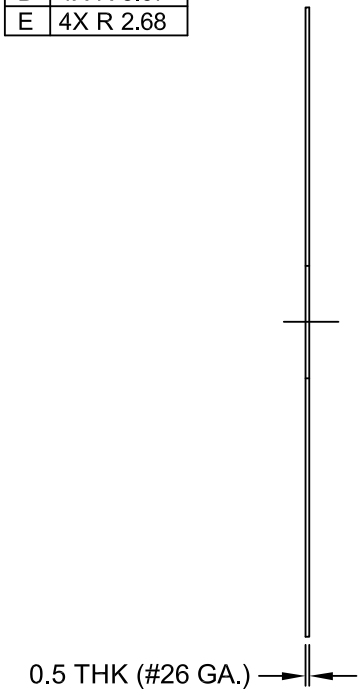

NOTES:

1. MATERIAL: M-19 NON-ORIENTED FULLY PROCESSED SILICON STEEL WITH C-5 CORE PLATE.
2. FLATNESS: 0.13 PER 25MM.
3. UNLESS OTHERWISE SPECIFIED ALL TOLERANCES ± 0.025.

DIMENSIONS ARE IN MM TOLERANCES UNLESS OTHERWISE SPECIFIED .X = ± 0.13 .XX = ± 0.025 ANGLE = ± 0° 30'	MOTORSOFT INC.			
	DWG	S.E.M.	8/20/02	TITLE: LAMINATION, ROTOR
	CHK	JRH	8/20/02	
	APPD	JRH	8/20/02	
USED ON: 2717	SCALE: 2 : 1			DWG. 2718 REV A

REV	ECO NO.	DATE	BY	APPD.
A	R0173	9/4/02	SEM	JRH

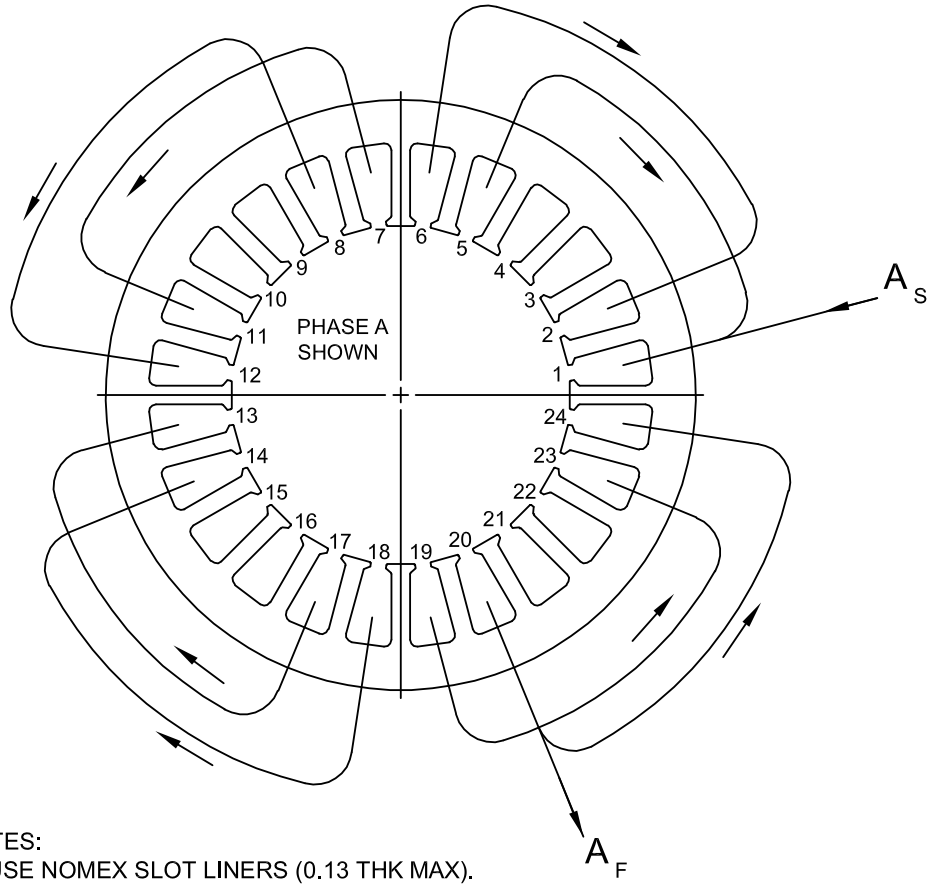

WINDING PATTERN

PHASE A		PHASE B		PHASE C	
IN	OUT	IN	OUT	IN	OUT
A S → 1	5	B S → 17	21	C S → 9	13
2	6	18	22	10	14
11	7	3	23	19	15
12	8	4	24	20	16
13	17	5	9	21	1
14	18	6	10	22	2
23	19	15	11	7	3
24	20 A F	16	12 B F	8	4 C F

WINDING SPECIFICATION

NUMBER OF PHASE	3 (A,B&C)
COILS/PHASE	8
TURNS/COIL	16
CONDUCTOR SIZE	#26 A.W.G. SINGLE BUILD
CONDUCTORS IN HAND	4

NOTES:
1. USE NOMEX SLOT LINERS (0.13 THK MAX).
2. NO INSULATION BETWEEN PHASES REQUIRED.
3. INSERT (1) THERMOCOUPLE DOWN CENTER OF SLOT BETWEEN PHASES A & B.
4. ENDTURNS TO BE BLOCKED, FORMED, LACED AND TRICKLE VARNISH.
5. MAGNET WIRE PIGTAILS SLEEVED WITH TEFLON.
6. HI POT TEST FOR 1000 V FOR 1 SECOND.
7. SURGE TEST FOR TURN TO TURN SHORTS.
8. TAG PHASES A, B & C STARTS AND FINISHES

ITEM	QTY	PART NO.	DESCRIPTION
1	1	1503	STACK, STATOR

PARTS LIST

DIMENSIONS ARE IN MM

TOLERANCES UNLESS OTHERWISE SPECIFIED
.X = ± 0.13
.XX = ± 0.025
ANGLE = ± 0° 30'

USED ON
2717

MOTORSOFT INC.

DWG	S.E.M.	8/15/02
CHK	JRH	8/20/02
APPD	JRH	8/20/02

TITLE
STATOR WINDING
(SYNCHRONOUS)

SCALE 1 : 1

DWG. 2719

REV A

REV	ECO NO.	DATE	BY	APPD.
A	R0170	8/30/02	SEM	JRH
B	R0172	9/4/02	SEM	JRH

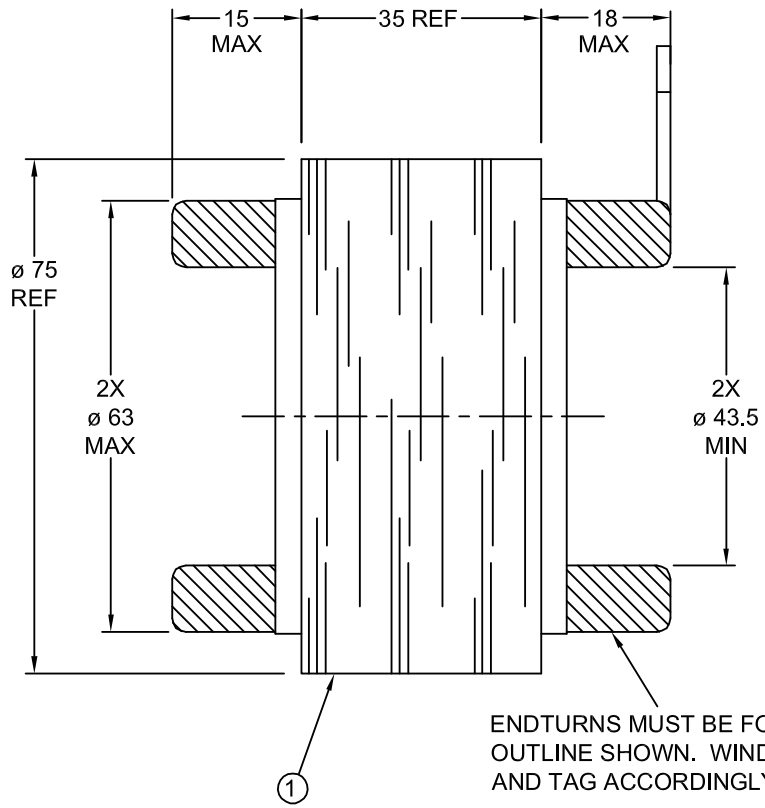

ENDTURNS MUST BE FORMED TO BE WITHIN OUTLINE SHOWN. WIND STATOR PER ITEM 1 AND TAG ACCORDINGLY.

(3) SET OF 2 MAGNET WIRE PIGTAILS
EACH PIG TAIL SLEEVED WITH TEFLON SLEEVING
(1) THERMOCOUPLE LEAD
BUNDLED TOGETHER WITH TEFLON SLEEVING
24" LG. MIN.

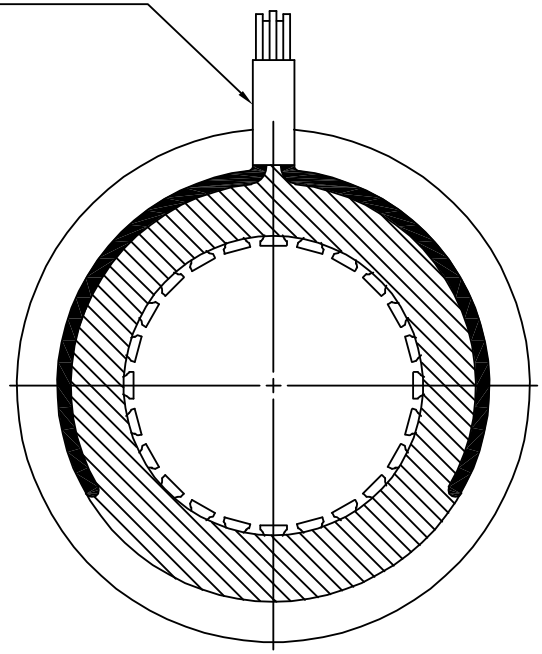

NOTES:

1. TRICKLE VARNISH AFTER FORMING ENDTURNS AND LACING.

ITEM	QTY	PART NO.	DESCRIPTION
1	1	2719	STATOR WINDING

PARTS LIST

DIMENSIONS ARE IN MM	MOTORSOFT INC.		
TOLERANCES UNLESS OTHERWISE SPECIFIED .X = ± 0.13 .XX = ± 0.025 ANGLE = ± 0° 30'	DWG S.E.M. 8/15/02 CHK JRH 8/20/02 APPD JRH 8/20/02	TITLE STATOR SUB-ASSY (SYNCHRONOUS)	
USED ON 2717	SCALE 1 : 1	DWG. 2720	REV B

REFERENCES

[1] Arefeen, M. S., Ehsani, M., and Lipo, T. A., "Sensorless position measurement in synchronous reluctance motor," *IEEE Transactions on Power Electronics*, vol. 9, pp. 624–630, Nov 1994.

[2] Betz, R. E., "Theoretical aspects of control of synchronous reluctance machines," in *IEE Proceedings*, vol. 139, pp. 355–364, 1992.

[3] Brown, R. H., Schneider, S. C., and Mulligan, M. G., "Analysis of algorithms for velocity estimation from discrete position versus time data," *IEEE Transactions on Industrial Electronics*, vol. 39, pp. 11–19, Feb 1992.

[4] Griffin, J., *The synchronous induction motor*. London: MacDonald and Co., 1954.

[5] Ha, J.-I., Kang, S.-J., and Sul, S.-K., "Position-controlled synchronous reluctance motor without rotational transducer," *IEEE Transactions on Industry Applications*, vol. 35, pp. 1393–1398, Nov/Dec 1999.

[6] Harnefors, L. and Isaksson, A. J., "Sensorless adaptive control of permanent-magnet motors: Some asymptotic properties," in *Proceedings of the American Control Conference*, (Albuquerque, NM), pp. 1203–1207, 1997.

[7] Javanovic, M. G., Betz, R. E., and Platt, D., "Sensorless vector controller for a synchronous reluctance machine," *IEEE Transaction on Industry Applications*, vol. 34, no. 2, pp. 346–354, 1998.

[8] Jones, L. A. and Lang, J. H., "A state observer for the permanent-magnet synchronous motor," *IEEE Transactions on Industrial Electronics*, vol. 36, no. 3, pp. 374–382, 1989.

[9] Khalil, H. K., *Nonlinear Systems*. Upper Saddle River, NJ: Prentice Hall, third ed., 2002.

[10] Krause, P. C., Wasynczuk, O., and Sudhoff, S. D., *Analysis of Electric Machinery*. New York, NY: IEEE Press, 1994.

[11] Kreindler, L., Testa, A., and Lipo, T., "Position sensorless synchronous reluctance motor drive using the stator phase voltage third harmonic," in *Conference Record of the 1993 IEEE Industry Applications Society Annual Meeting*, vol. 1, (Toronto, Ontario, Canada), pp. 679–686, Oct 1993.

[12] Lagerquist, R., Boldea, I., and Miller, T. J. E., "Sensorless control of the synchronous reluctance motor," *IEEE Transactions on Industry Applications*, vol. 30, pp. 673–682, May/Jun 1994.

[13] Lawrenson, P. J. and Agu, L. A., "Low inertia reluctance machines," in *Proceedings of the IEE*, vol. 111, pp. 2017–2025, Dec 1964.

[14] Lawrenson, P. J. and Gupta, S. K., "Development in the performance and theory of segmental-rotor reluctance motors," in *Proceedings of the IEE*, vol. 114, pp. 645–653, May 1967.

[15] Lewis, F. L. and Syrmos, V. L., *Optimal Control*. New York, NY: John Wiley and Sons, Inc., second ed., 1995.

[16] Lipo, T., "Synchronous reluctance machines - a viable alternative for ac drives," *Electric Machines and Power Systems*, vol. 19, no. 6, pp. 659–671, 1991.

[17] Matsuo, T. and Lipo, T. A., "Rotor position detection scheme for synchronous reluctance motor based on current measurements," *IEEE Transactions on Industry Applications*, vol. 31, no. 4, pp. 860–868, 1995.

[18] Schroedl, M. and Weinmeier, P., "Sensorless control of reluctance machines at arbitrary conditions including standstill," *IEEE Transactions on Power Electronics*, vol. 9, pp. 225–231, Mar 1994.

VITA

Matthew Hortman was born in Macon, Georgia, in 1974 and grew up on a farm in Roberta, a small rural community outside Macon.

In 1998 he received a B.S. in Engineering and a B.A. in Computer Science from Mercer University, also in Macon. During the time at Mercer, Matt earned five quarters of co-op experience working for CEGELEC Automation, a motor drives company, and TASC, a defense contractor. Both jobs provided an equal amount of programming and engineering experience.

After graduation, Matt answered the call of a steady paycheck and accepted a position with Advanced Systems Integration, a small systems integration company based in Alpharetta, Georgia, and spent almost four years writing software for a variety of projects but doing very little actual engineering work. In 2001, he decided to return to engineering and began graduate studies at Georgia Institute of Technology in Atlanta, Georgia.

His research interests are varied and include embedded, real-time, and distributed software, simulation, motor and motion control, power electronics and scientific data processing and visualization.